Micromechanical modelling for effect of inherent anisotropy on cyclic behaviour of sand

Zhen-Yu Yin [a,*], Ching S. Chang [b], Pierre-Yves Hicher [c]

[a] Department of Civil Engineering, Shanghai Jiaotong University, Shanghai, People's Republic of China
[b] Department of Civil and Environmental Engineering, University of Massachusetts, Amherst, MA 01002, USA
[c] Research Institute in Civil and Mechanical Engineering, GeM UMR CNRS 6183, Ecole Centrale de Nantes, BP 92101, 44321 Nantes Cédex 3, France

ABSTRACT

The inherent anisotropy more or less exists in sand when preparing samples in laboratory or taking from field. The purpose of this paper is to model cyclic behaviour of sand by means of a micromechanical approach considering inherent anisotropy. The micromechanical stress–strain model developed in an earlier study by Chang and Hicher (2005) is enhanced to account for the stress reversal on a contact plane and the density state-dependent dilatancy. The enhanced model is first examined by simulating typical drained and undrained cyclic tests in conventional triaxial conditions. The model is then used to simulate drained cyclic triaxial tests under constant p' on Toyoura sand with different initial void ratios and different levels of p', and undrained triaxial tests on dense and loose Nevada sand. The applicability of the present model is evaluated through comparisons between the predicted and the measured results. The evolution of local stresses and local strains at inter-particle planes due to externally applied load are discussed. All simulations have demonstrated that the proposed micromechanical approach is capable of modelling the cyclic behaviour of sand with inherent and induced anisotropy.

© 2010 Elsevier Ltd. All rights reserved.

1. Introduction

Cyclic behaviour of sand has been widely studied during last decades, e.g., Ishihara et al. (1975), Matsuoka et al. (1985), Pradhan et al. (1989), Arulmoli et al. (1992), Hyodo et al. (1994), Koseki et al. (2000), Qadimi and Coop (2007), etc. In general, during drained cyclic test, loose sand densifies and dense sand dilates; during undrained cyclic test, loose sand liquefies, and dense sand exhibits accumulated deformation.

The models that can describe cyclic behaviour of sand have been developed mainly through the elasto-plastic approach, such as Dafalias and Herrmann (1982), Bardet (1985), Balendran and Nemat-Nasser (1993), Manzari and Dafalias (1997), Oka et al. (1999), Park and Desai (2000), Wan and Guo (2001), Setouchi et al. (2005), López-Querol and Blázquez (2006), Yu et al. (2007), Anandarajah (2008), etc.

Although cyclic behaviour of sand have been extensively studied using elasto-plastic models for a soil element, two aspects of the soil behaviour have rarely been investigated in the literature: (1) the slip mechanism at inter-particle contact level has not been explicitly considered in the model. This consideration is useful for

modelling soil under more complex stress such as cyclic loading, and (2) the effect of inherent anisotropy on cyclic behaviour of sand has rarely been discussed. Consideration of this effect is imperative since sand is often anisotropic due to its geological formation process.

In order to tackle theses two aspects, a micromechanics approach (e.g., Chang and Hicher, 2005) is a suitable way to be adopted. In this approach, the deformation of an assembly can be obtained by integrating the movement of the inter-particle contacts in all orientations. The orientation-dependent properties of soil can be explicitly represented, thus the inherent anisotropy can be physically characterized in a more direct way.

In this paper, we extend the model of Chang and Hicher (2005) to be capable of simulating soils under cyclic loading. We introduce a formulation accounting for the stress reversal on inter-particle plane and introducing a density-dependent dilatancy relation to account for the effect due to cyclic densification. This newly developed model is capable of simulating behaviour from micro-level (contact planes) to macro-level (assembly) including inherent and induced anisotropy of sand under cyclic loading conditions.

In what follows, based on the model of Chang and Hicher (2005), the newly introducing formulations for reverse loading and the density state effect on the stress dilatancy relation are described and demonstrated using cyclic test results of sand under both drained and undrained conditions, with the effect of inherent

* Corresponding author. Tel./fax: +86 21 62932915.
E-mail addresses: zhenyu.yin@gmail.com, zhenyu.yin@ec-nantes.fr (Z.-Y. Yin), chang@ecs.umass.edu (C.S. Chang), pierre-yves.hicher@ec-nantes.fr (P.-Y. Hicher).

cross-anisotropy. Then, a series of experimental results on Toyoura sand and Nevada sand are used for further verification of this approach. The evolution of local stresses and local strains at inter-particle planes due to externally applied load are also discussed. The overall applicability of the present model is evaluated based on the comparison of measured and predicted results.

2. Enhanced model for cyclic behaviour of sand

Chang and Hicher (2005) have developed a micromechanics-based model, which has been applied to monotonic triaxial tests on sand specimens under both drained and undrained conditions. For cyclic load conditions, modified formulations for reverse loading on a contact plane are required that incorporate the effect of cyclic densification. In this section, we present the modified formulations of the model. Basic formulations of the model by Chang and Hicher (2005) are summarized in Appendix A.

2.1. Modification for reverse loading

Upon shear reversal, the direction of sliding on each inter-particle plane is reversed. At the moment of shear reversal, the plastic displacements δ_s^{pR}, δ_t^{pR}, and the forces f_n^R, f_s^R, f_t^R (see Fig. 1 for local coordinate system n–s–t), are regarded as reversal state variables of the contacts. The reversal state has a significant influence on the subsequent sliding behaviour. Thus, we take account of the reversal state variables in the hardening equation and the dilatancy equation as follows:

$$\kappa = \frac{k_{p0}\tan\phi_p^*\delta_r^{p*}}{\tan\phi_p^* + k_{p0}\delta_r^{p*}} \quad (1)$$

$$\begin{Bmatrix} d\delta_n^p \\ d\delta_s^p \\ d\delta_t^p \end{Bmatrix} = d\delta_r^p \begin{Bmatrix} D\left[\tan\phi_0 - \frac{1}{\tan\phi_m^*}\left(\frac{f_s}{f_n}\right)^*\left(\frac{f_s}{f_n}\right) - \frac{1}{\tan\phi_m^*}\left(\frac{f_t}{f_n}\right)^*\left(\frac{f_t}{f_n}\right)\right] \\ \frac{1}{\tan\phi_m^*}\left(\frac{f_s}{f_n}\right)^* \\ \frac{1}{\tan\phi_m^*}\left(\frac{f_t}{f_n}\right)^* \end{Bmatrix} \quad (2)$$

Note that these two equations carry the same form as the previous equations (Eqs. (A6) and (A8)). The only difference is the superscript (*) marked on the plastic shear displacement δ^{p*}, the mobilized force ratios $(f_s/f_n)^*$, $(f_t/f_n)^*$, the mobilized friction angle ϕ_m^* and the peak friction angle ϕ_p^*, which are defined below to include the effect of the reversal state variables:

$$\delta_r^{p*} = \sqrt{\left(\delta_s^p - \delta_s^{pR}\right)^2 + \left(\delta_t^p - \delta_t^{pR}\right)^2} \quad (3)$$

$$\left(\frac{f_s}{f_n}\right)^* = \frac{f_s}{f_n} - \frac{f_s^R}{f_n^R}, \quad \left(\frac{f_t}{f_n}\right)^* = \frac{f_t}{f_n} - \frac{f_t^R}{f_n^R},$$
$$\tan\phi_m^* = \sqrt{\left(\frac{f_s}{f_n} - \frac{f_s^R}{f_n^R}\right)^2 + \left(\frac{f_t}{f_n} - \frac{f_t^R}{f_n^R}\right)^2} \quad (4)$$

$$\tan\phi_p^* = \sqrt{\left(\frac{\tan\phi_p}{\tan\phi_m^*}\left(\frac{f_s}{f_n}\right)^* - \frac{f_s^R}{f_n^R}\right)^2 + \left(\frac{\tan\phi_p}{\tan\phi_m^*}\left(\frac{f_t}{f_n}\right)^* - \frac{f_t^R}{f_n^R}\right)^2} \quad (5)$$

A schematic explanation of the effects of reverse state is shown in Fig. 2. According to Fig. 2, the effect of stress reversal at a contact
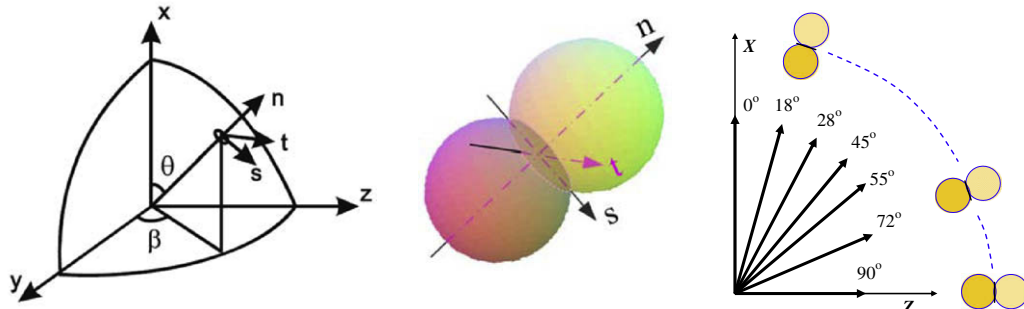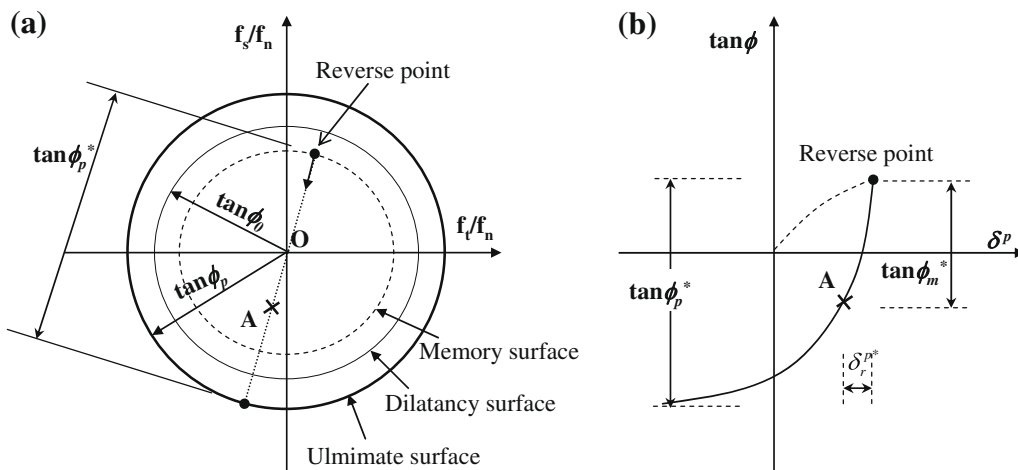

Fig. 1. Local coordinate at inter-particle contact.

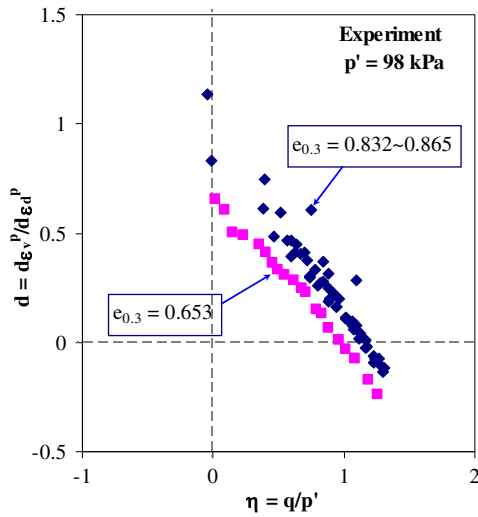**Fig. 2.** Principle of the force reversal.

Fig. 3. Evolution of stress dilatancy at constant p' for virgin loading (after Pradhan et al., 1989).

plane is considered by the modification of $\tan\phi_p$ to $\tan\phi_p^*$ in hardening equation (Eq. (5)). Here, the two terms $(f_s/f_n)/\tan\phi_m$ and $(f_t/f_n)/\tan\phi_m$ in Eq. (A8) are modified to $(f_s/f_n)^*/\tan\phi_m^*$ and $(f_t/f_n)^*/\tan\phi_m^*$ in Eq. (2) to account for the effect of stress reversal for plastic flow rule.

Eq. (2) indicates that the amount of dilatancy is different upon shear reversal. This concept is similar to that proposed by Balendran and Nemat-Nasser (1993) and Wan and Guo (2001). Eq. (1) suggests that the same form of hardening rule can be used for both loading and unloading conditions, but requires some scaling process on the value of $\tan\phi_p$. This concept is similar to that used in Masing's rule and in bounding surface plasticity (Dafalias and Herrmann, 1982).

2.2. Modification for dilatancy equation with density state-dependency

Pradhan et al. (1989) carried out drained constant-p' tests under cyclic loading on Toyoura sand for various values of p' and various soil densities. Fig. 3 shows the curves of stress dilatancy, plotted on a plane of strain ratio $d\varepsilon_v^p/d\varepsilon_d^p$ (contraction in positive) versus stress ratio $\eta = q/p'$, for the virgin loading on specimens of Toyoura sand with two different densities ($e_{0.3} = 0.845$ and $e_{0.3} = 0.653$ where $e_{0.3}$ is the void ratio under isotropic compression with $p' = 30$ kPa). The results demonstrate that the dilatancy curves are two different lines for dense and loose sands. Comparing to loose sand, the dense sand have a lower value of stress ratio η when $d\varepsilon_v^p/d\varepsilon_d^p = 0$, which implies having a lower value of phase transformation angle ϕ_0.

In Fig. 4, the dilatancy curves are also plotted for several cycles using the same experimental measurements by Pradhan et al. (1989) for loose sand under four different mean stress p'. It can be observed from Fig. 4 that, the dilatancy curves are unconnected
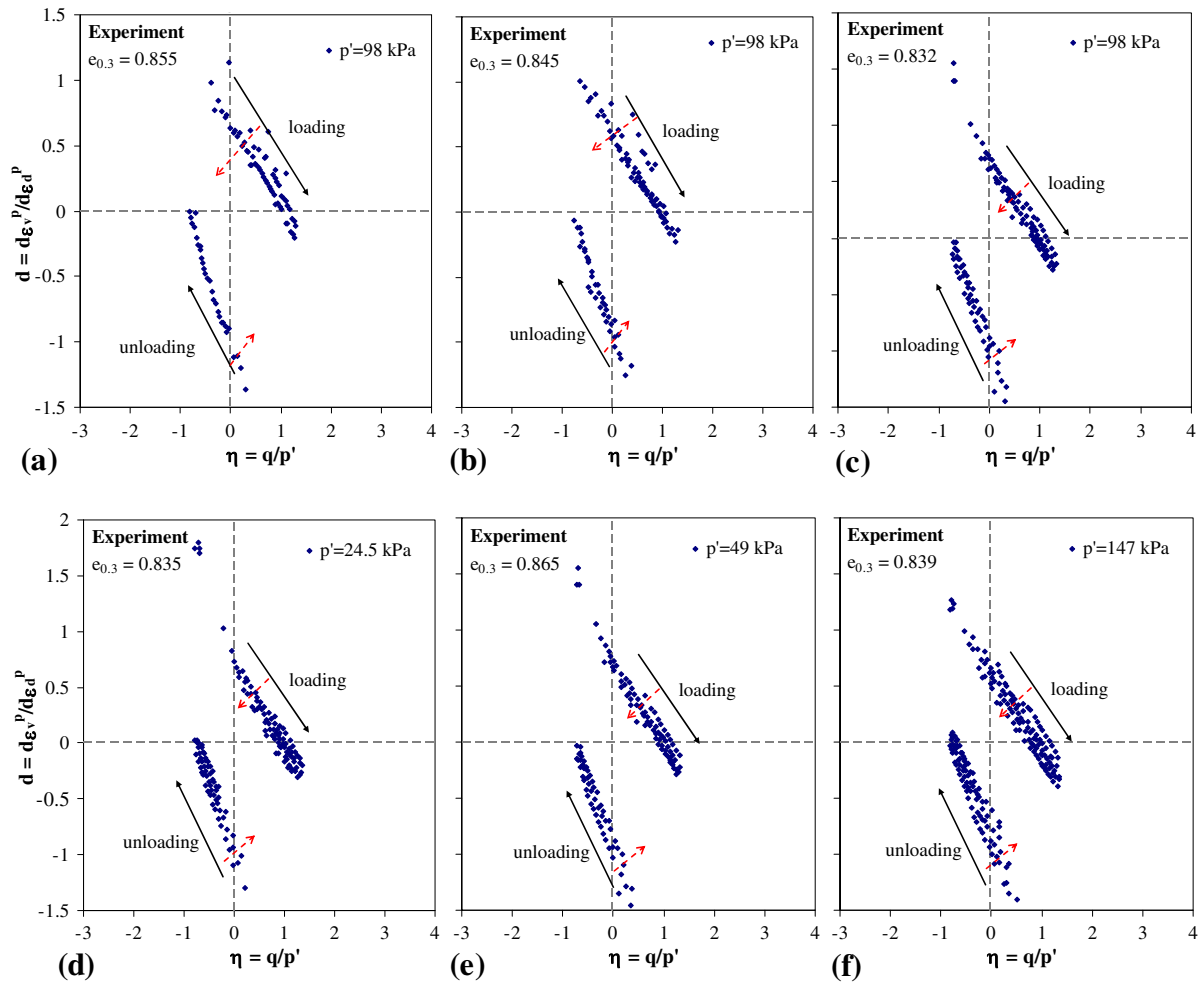

Fig. 4. Evolution of stress dilatancy during cyclic loading at constant p' (after Pradhan et al., 1989).
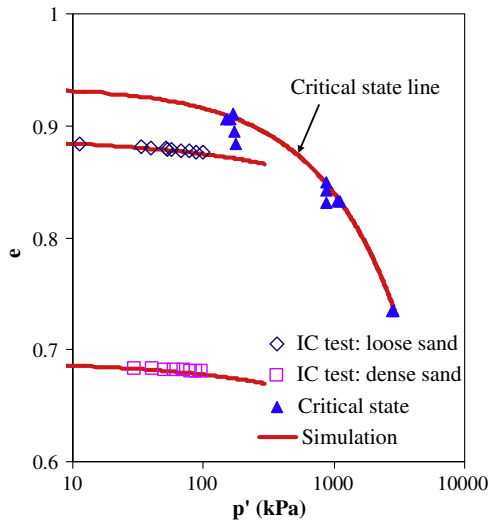
Fig. 5. Critical state line and isotropic compression line in e–$\log p'$-plane for Toyoura sand.

for loading stages and unloading stages during the cyclic load. Furthermore, in either loading or unloading stages, the dilatancy curves are also different for each cycle of load; $\tan \phi_0$ decreases with cyclic densification. Therefore, even for the same sand, the dilatancy curves are affected by both the loading direction and the cyclic densification.

These experimental observations are for a soil element. Unfortunately, no dilatancy measurements at inter-particle level are available at present time. Nevertheless, these observations suggest that at inter-particle level, the effect of density state on the stress dilatancy should be taken into account in addition to the effect of residual state. Eq. (2) is thus modified as follows:

$$\frac{d\delta_n^p}{d\delta_r^p} = D(\tan \phi_0 - \tan \phi_m^*) \exp\left[h\left(\frac{e}{e_c} - 1\right)\right] \qquad (6)$$

where h is material constant for the effect of density state on the stress dilatancy.

The local phase transformation line $\tan \phi_0$ depends not only on the internal friction angle ϕ_μ, but also on the density state. Jefferies (1993) proposed a state parameter $(e - e_c)$ dependent phase transformation line. Here, we use the density state of packing proposed by Biarez and Hicher (1994):

$$\tan \phi_0 = \left(\frac{e_c}{e}\right)^{-m} \tan \phi_\mu \qquad (7)$$

This relationship allows a dense packing to dilate at earlier stage of shear loading.

2.3. Parametric study

The newly introduced dilatancy equation for the model is examined by predicting a typical drained cyclic triaxial test on loose sand ($e_0 = 0.86$) under $\sigma_r' = 100$ kPa with a constant axial strain amplitude ±1.5%. The parameters used for the parametric

study are based on typical results from Toyoura sand (see Table 1, details in Section 4.1.1).

To highlight the effect of cyclic densification, comparisons were made for the effect of parameter D, and the effect of parameter h. Fig. 6(a)–(c) shows the predicted behaviour of drained cyclic test ($D = 1$, and $h = 0$). Fig. 6(c) and (d) shows the evolution of stress dilatancy for $D = 0.5$, 1, and 1.2 under $h = 0$, and Fig. 6(e)–(f) for $h = 5$ and 10 under $D = 1$. The comparisons demonstrate that the parameter D controls the amount of dilatancy in monotonic loading, while the parameter h controls the accumulated dilatancy during cyclic loading due to densification.

To present the coupling effect of parameters D and h, two sets of dilatancy constants were used: (i) $D = 1$ and $h = 0$; (ii) $D = 1.354$ and $h = 5$. Since these two sets of parameters would give exactly the same dilatancy in the beginning of virgin loading (see Eq. (6)) with confining stress = 100 kPa, $e = 0.86$ and $e_c = 0.915$), thus, the predicted difference would show the effect of cyclic densification. Fig. 6(a) and (g) shows the response of stress ratio versus axial strain, which indicate that the effect of cyclic densification is not important for predicted shear strain. Fig. 6(b) and (h) shows the response of volumetric strain versus axial strain; the volumetric strains for the cases with $h = 5$ and 0 are very different due to the cyclic densification effect. The evolution of stress dilatancy for the case with $h = 5$ (see Fig. 6i) by the enhanced model, compared to that for the case with $h = 0$ (see Fig. 6c), captured the experimentally measured trend of stress dilatancy during cyclic loading (see Fig. 4).

3. Effect of inherent anisotropy

As a result of the deposition process and the elongated particle shape, sand usually exhibits horizontal bedding planes, which are the sources of inherent anisotropy. The inherent anisotropy usually affects on two material constants, namely (1) contact stiffness k_{n0}, and (2) friction angle ϕ_μ. To highlight these effects, soil behaviour for two typical loading conditions was generated: one is as presented in the previous section under drained condition, and the other is undrained cyclic test on loose sand ($e_0 = 0.86$) under $\sigma_r' = 100$ kPa with a constant deviatoric stress amplitude (from 15 kPa to −10 kPa). The parameters of Toyoura sand in Table 1 were used for the investigation.

3.1. Effect of inherent anisotropy of stiffness

For cross-anisotropy of normal elastic stiffness k_{n0} with three different values in principal axes k_{n0}^{11}, k_{n0}^{22} and k_{n0}^{33}, a second-order tensor form can be written as:

$$\left[k_{n0}^{ij}\right] = \begin{bmatrix} k_{n0}^{11} & 0 & 0 \\ 0 & k_{n0}^{22} & 0 \\ 0 & 0 & k_{n0}^{33} \end{bmatrix} = k_{n0}^{ave} \begin{bmatrix} 1 + a_0 & 0 & 0 \\ 0 & 1 - \frac{a_0}{2} & 0 \\ 0 & 0 & 1 - \frac{a_0}{2} \end{bmatrix} \qquad (8)$$

where $k_{n0}^{ave} = \left(k_{n0}^{11} + k_{n0}^{22} + k_{n0}^{33}\right)/3$. The orientation distribution of the normal elastic stiffness for a cross-anisotropic case is (Chang and Misra, 1990):

Table 1
Values of parameters for very Toyoura sand and Nevada sand.

Parameters	Global parameters			Inter-particle parameters						
	λ	e_{ref}	ξ	D	h	ϕ_μ' (°)	n	k_{n0} (MPa)	k_{rR}	k_{pR}
Toyoura sand	0.019	0.934	0.7	1	5	31[a]	0.5	12.5[a]	0.5	0.15
Nevada sand	0.015	0.79	0.7	2	5	32.3	0.5	9.8[a]	0.5	0.3

[a] Average value.

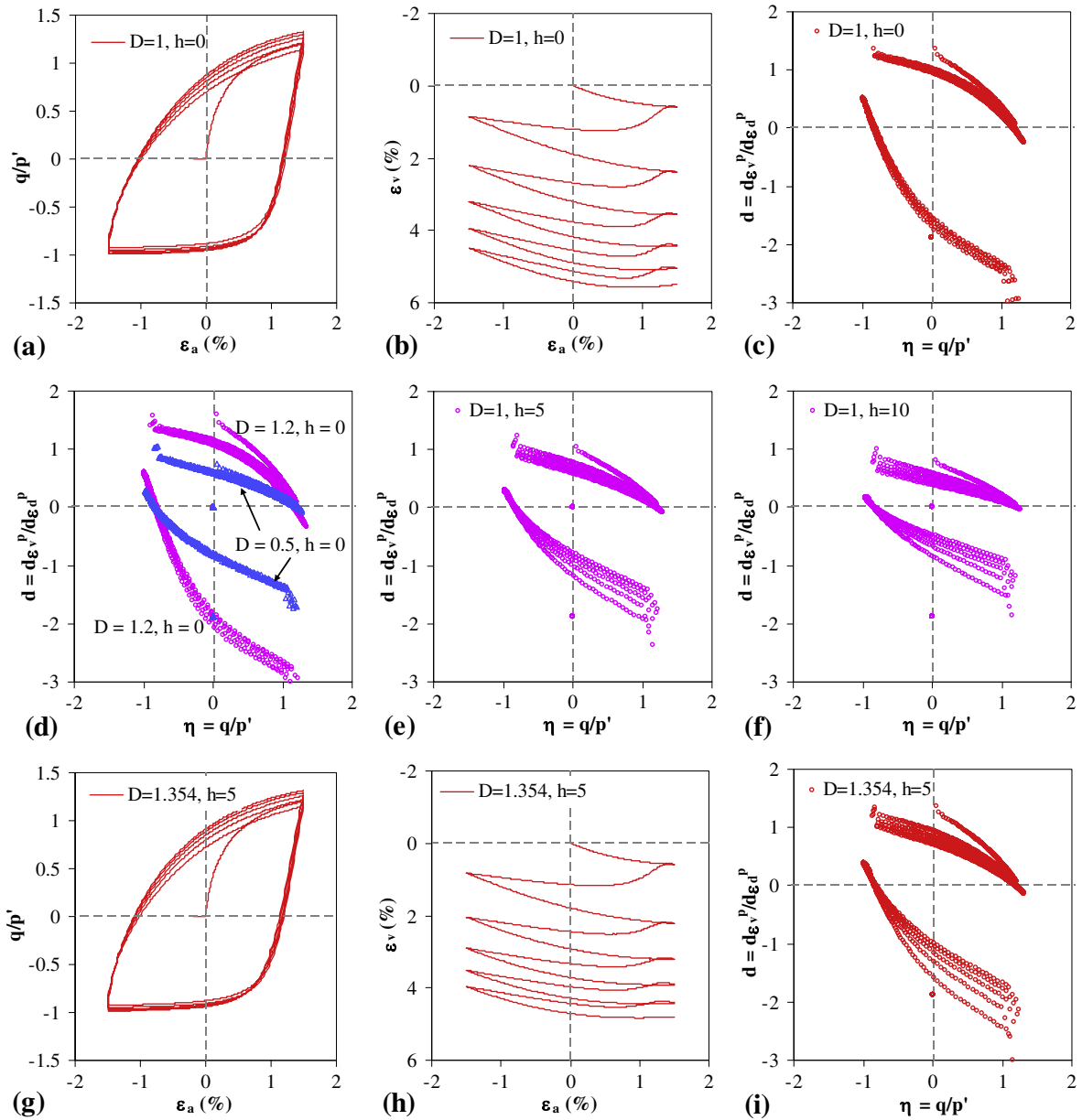**Fig. 6.** Numerical simulation for drained triaxial cyclic test on Toyoura sand (e_0 = 0.86, σ'_r = 100 kPa).

(a) k_{n0}^{ave} = 12.5 N/mm, a_0 = 0   (b) k_{n0}^{ave} = 12.5 N/mm, a_0 = 0.8   (c) in X-Z plane
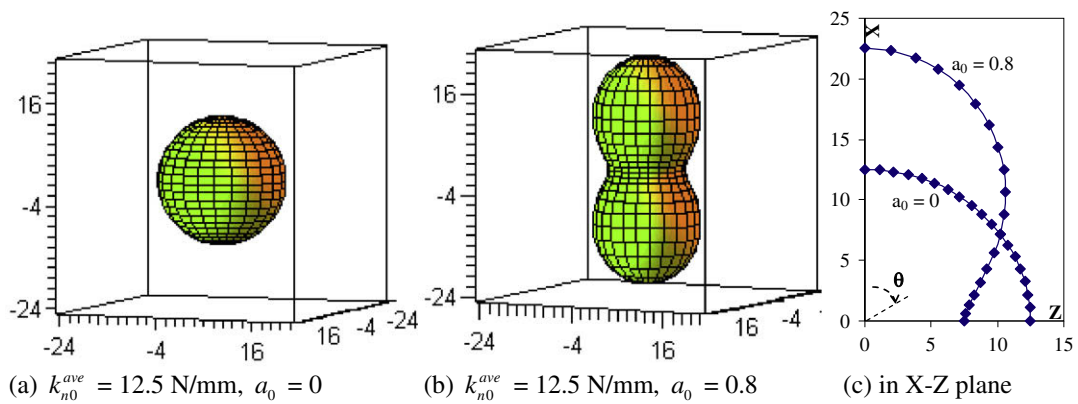
Fig. 7. Schematic plot for orientation distribution of inherited anisotropy of normal elastic modulus.
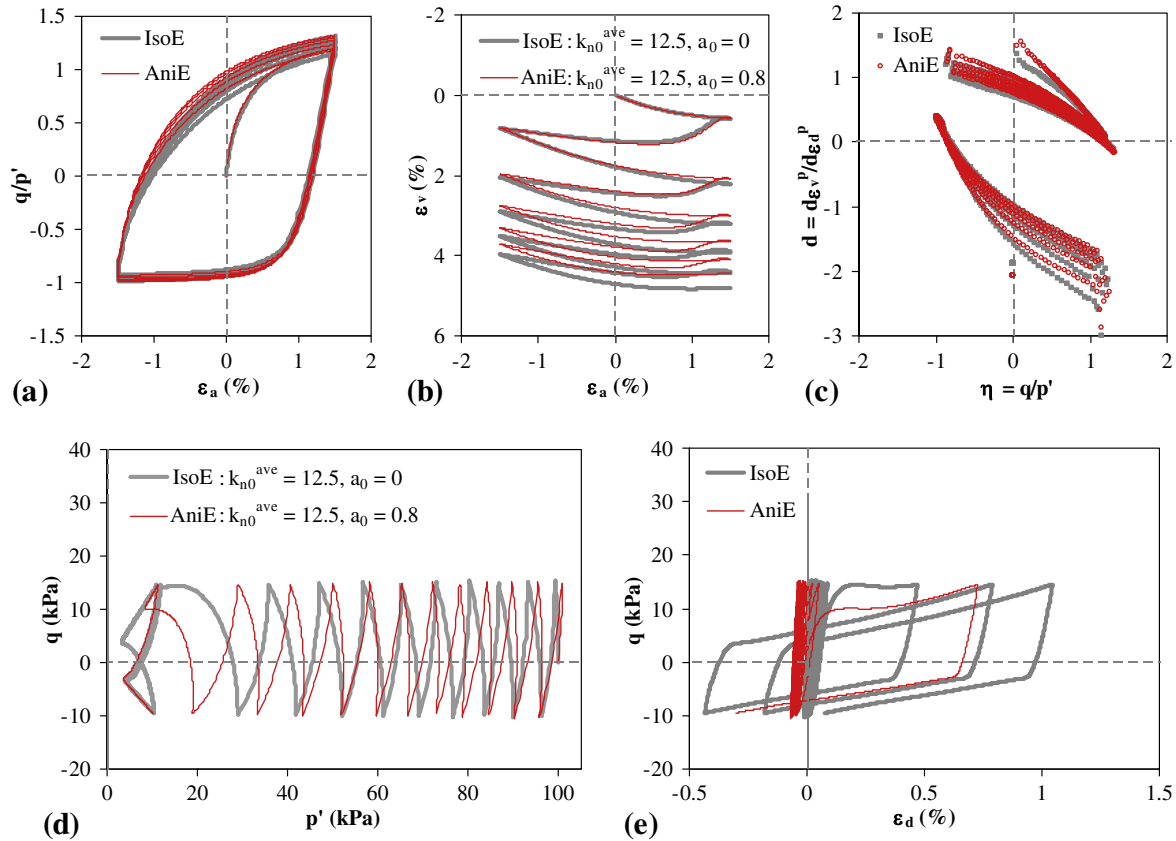
Fig. 8. Numerical simulations for drained and undrained triaxial cyclic test by model considering isotropic and inherent anisotropic stiffness.
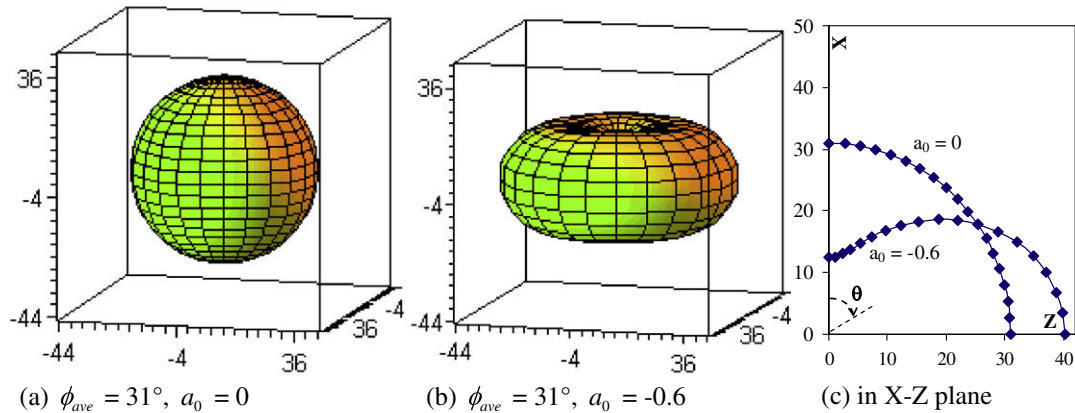

Fig. 9. Schematic plot for orientation distribution of inherited anisotropy of friction angle.

$$k_{n0}(\theta) = k_{n0}^{ave}\left(1 + \frac{a_0}{4}(3\cos 2\theta + 1)\right) \qquad (9)$$

where the angle θ is defined in Fig. 1 in a spherical coordinate. In this cross-anisotropic case, the orientation distribution is symmetrical about its major axis that coincides with z-direction (the vertical direction).

Since the elastic shear stiffness k_r (by k_{rR}) and plastic stiffness k_p (by k_{pR}) are dependent on normal elastic stiffness k_n (Eqs. (A3) and (A7)). Thus, the inherent anisotropy also includes both elastic and plastic shear stiffness.

In order to investigate the effect of inherent anisotropy of stiffness on the cyclic behaviour, we assume $k_{n0}^{ave} = 12.5$ N/mm and the

anisotropic constant $a_0 = 0.8$ (or the three principal values for k_{n0} : $k_{n0}^{11} = 22.5$ N/mm, $k_{n0}^{22} = k_{n0}^{33} = 7.5$ N/mm with horizontal bedding plane). The orientation distribution of the normal elastic stiffness is obtained by Eq. (9), as shown in Fig. 7 (in spherical coordinate as Fig. 1).

Fig. 8 shows the comparison between simulated results with isotropic stiffness and those with inherent anisotropic stiffness for drained and undrained cyclic behaviours. For loading stages, the inherent anisotropic stiffness (stiffer in vertical direction shown in Fig. 7) gives stiffer slope of the curves of stress ratio versus axial strain than that of isotropic stiffness (see Fig. 8a). For unloading stages, very little difference exists between two cases. Similar phenomenon is also obtained for volumetric strains (see
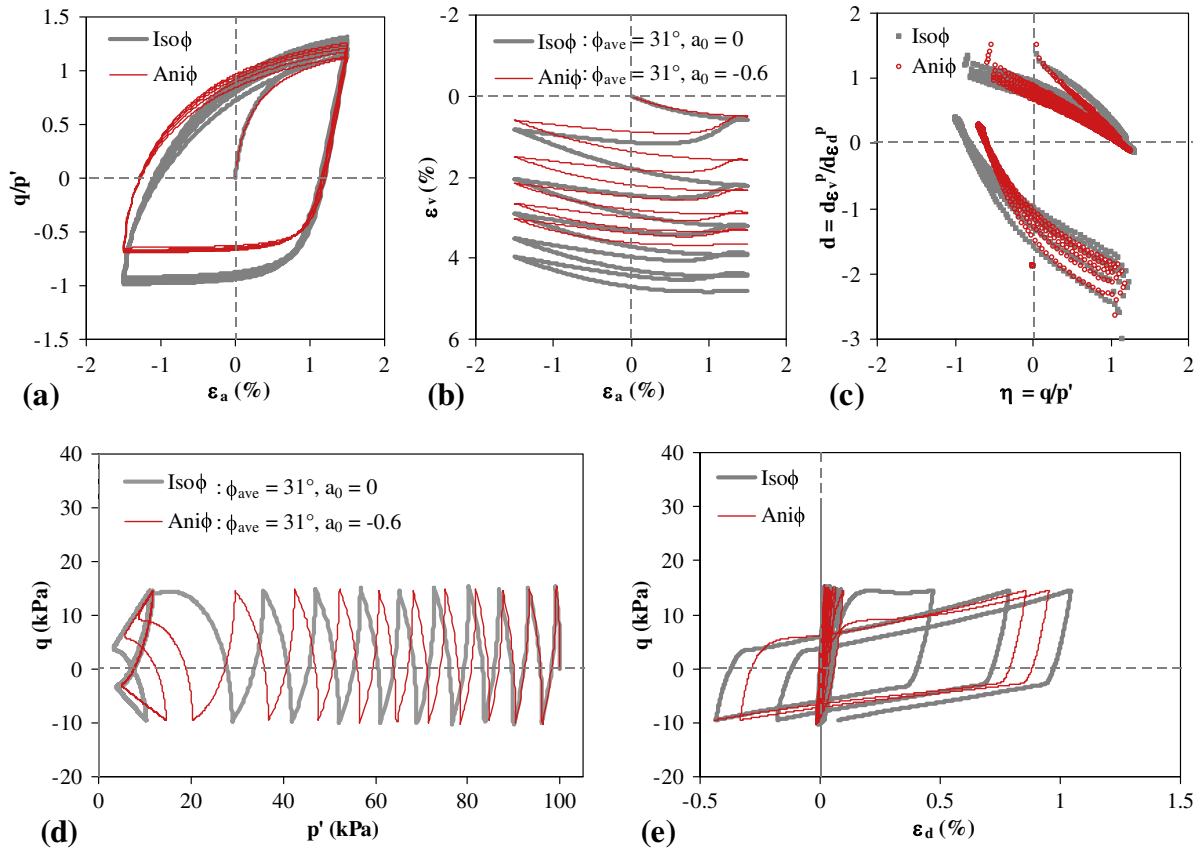
Fig. 10. Numerical simulations for drained and undrained triaxial cyclic test by model considering isotropic and inherent anisotropic friction angle.
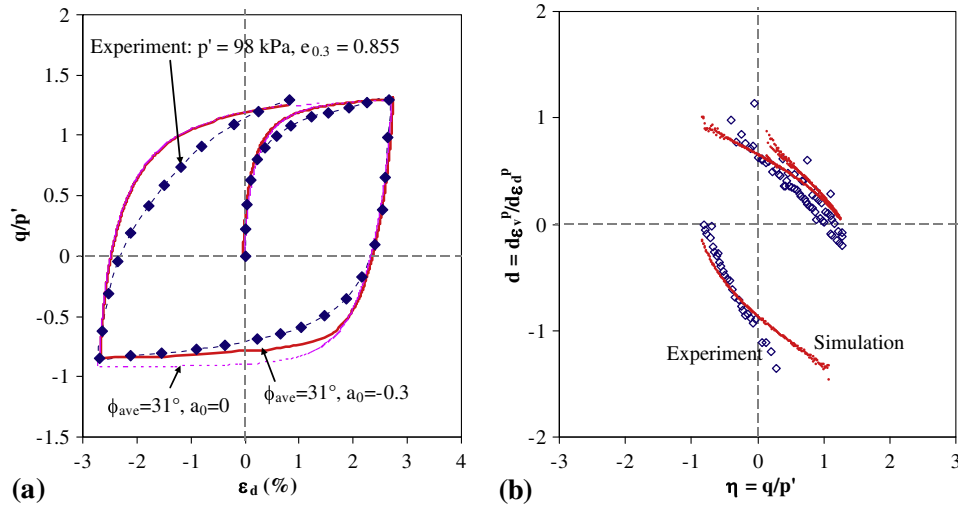

Fig. 11. Simulations for drained constant p' triaxial tests with loading, unloading and reloading stages on Toyoura sand.

Fig. 8b): less volumetric strains occur during loading stages agreeing with stiffer slope of stress–strain curves. For the stress dilatancy, the inherent anisotropic stiffness gives a little higher transformation angle than that of isotropic case for loading stages and smaller transformation angle for unloading stages (see Fig. 8c).

As expected, the assumed anisotropic contact stiffness leads to the modulus of vertical direction larger than that of horizontal direction, i.e., $E_v/E_h > 1$, as shown by Hicher and Chang (2006). As a result, for undrained response, less excess pore pressure occurs during loading stages and inversely during unloading stages (see Fig. 8d). This is also in agreement with the results obtained by Dakoulas and Yu (1995). Fig. 8(e) shows the stress–strain response during undrained cyclic loading. The large strain occurs starting from the ninth cycle for the case of isotropic stiffness and from the 11th cycle for the anisotropic case. In general, the slope of stress–strain curves during loading stages for anisotropic case is stiffer than that of isotropic case, as shown for drained cyclic test in Fig. 8a.
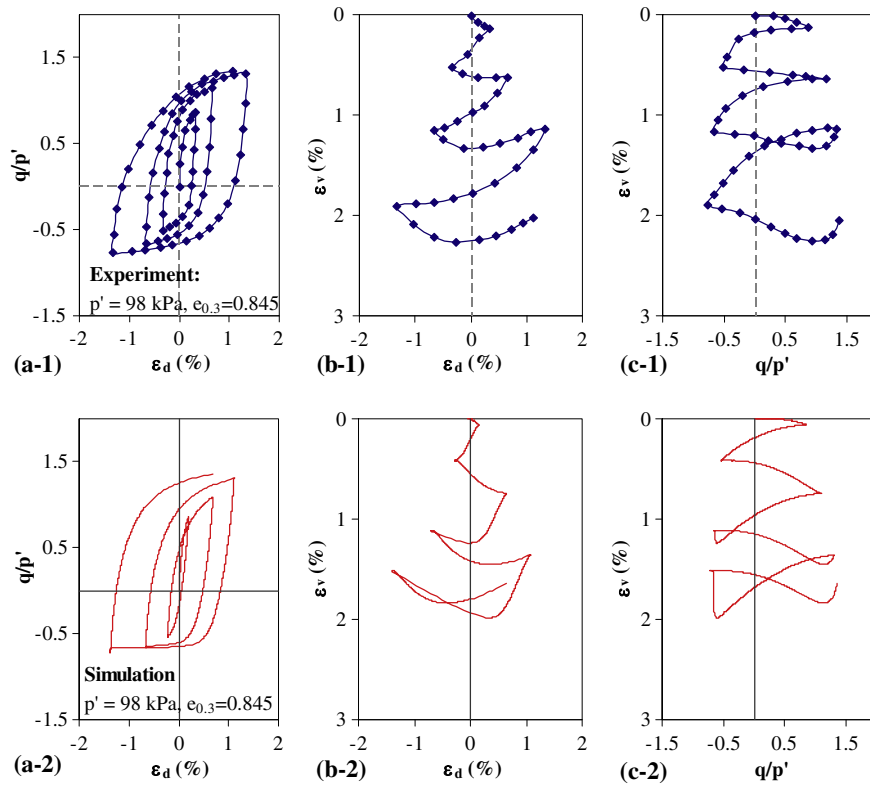
Fig. 12. p'-Constant drained cyclic test on loose Toyoura sand ($e_0 = 0.845$).
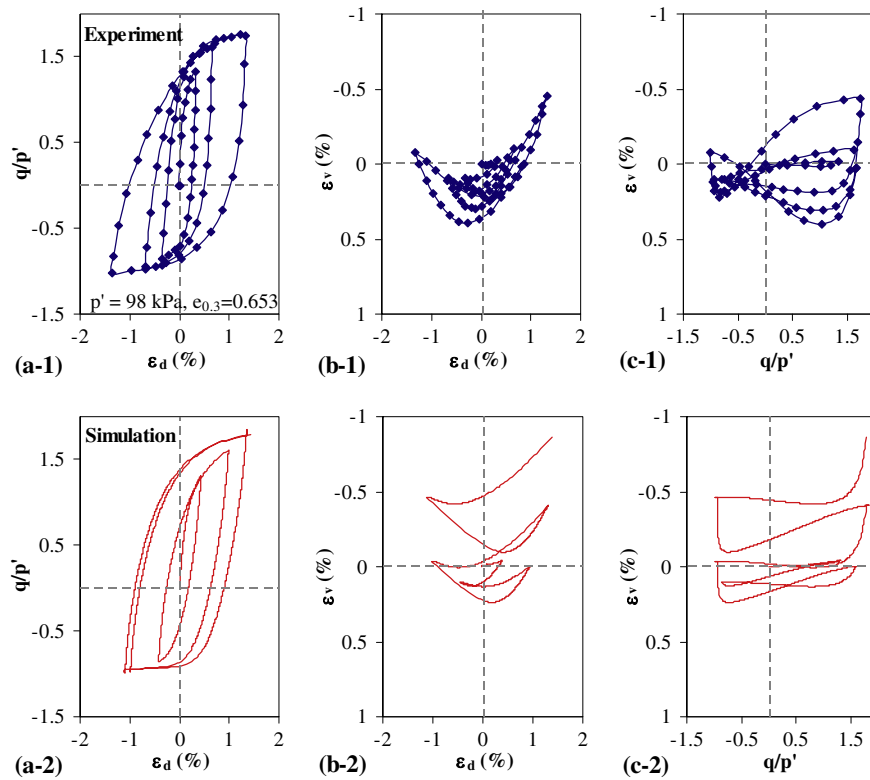
Fig. 13. p'-Constant drained cyclic test on dense Toyoura sand ($e_0 = 0.653$).

3.2. Effect of inherent anisotropy of friction angle

Similar to normal elastic stiffness, the cross-anisotropy of friction angle ϕ can be described in a form similar to Eq. (8). We assume $\phi_{ave} = 31°$ and the anisotropic constant $a_0 = -0.6$ (or the three principal values for ϕ: $\phi_{11} = 12.4°$, $\phi_{22} = \phi_{33} = 40.3°$ for horizontal bedding plane). The orientation distribution of the friction angle is obtained by

Fig. 14. p'-Constant drained cyclic tests on loose Toyoura sand.

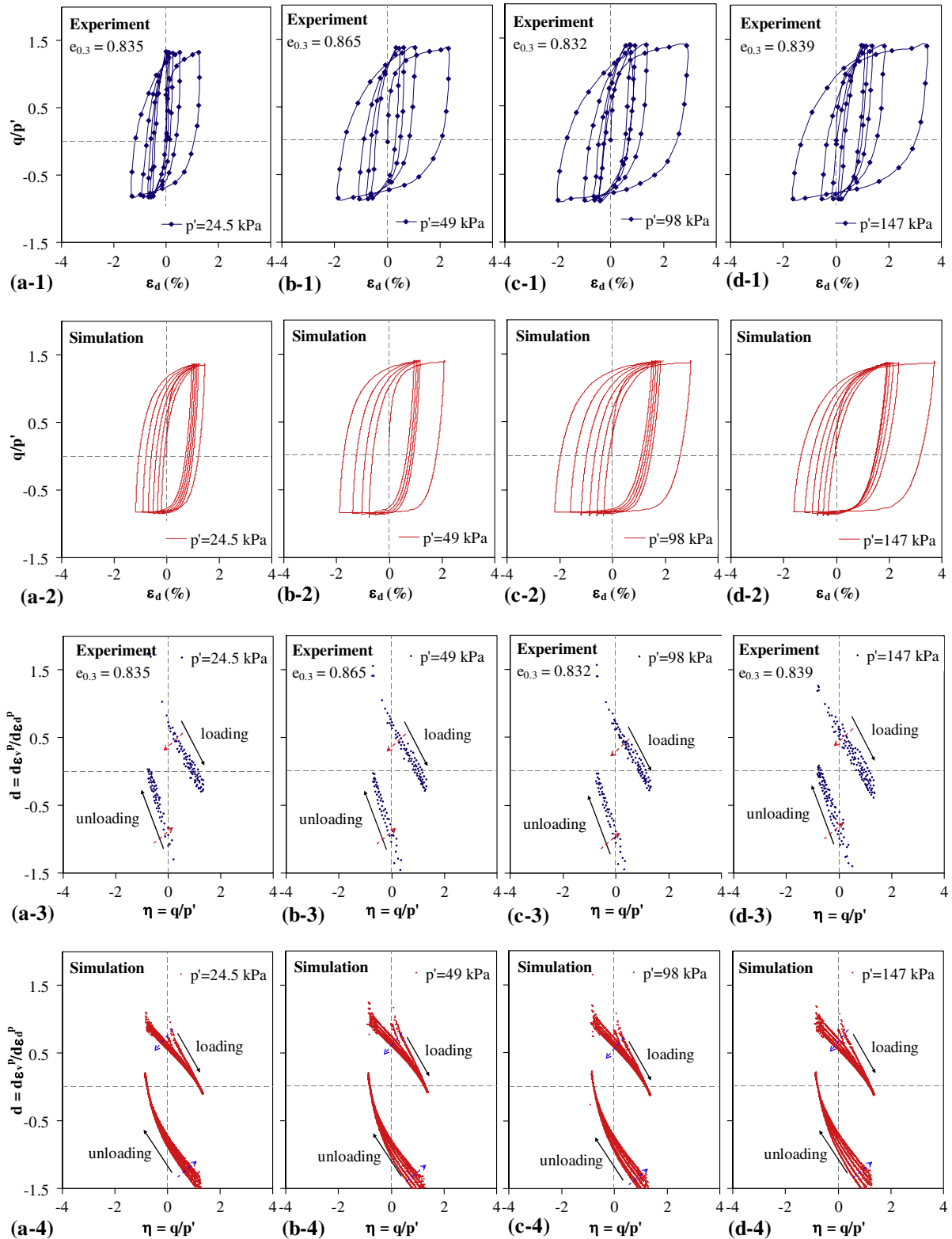$$\phi_\mu(\theta, \beta) = \phi_\mu^{ave}\left(1 + \frac{a_0}{4}(3\cos 2\theta + 1)\right) \qquad (10)$$

and is shown in Fig. 9 (in spherical coordinate as Fig. 1).

Fig. 10 shows the comparison between the simulated results with isotropic friction angle and those with inherent anisotropic friction angle for drained and undrained cyclic behaviours. For

unloading stages, the inherent anisotropic friction angle (larger in horizontal direction shown in Fig. 9) gives smaller strength than that of isotropic case (see Fig. 10a). For loading stages, very little difference exists between the isotropic and anisotropic cases. The volumetric strains (see Fig. 10b) are significantly influenced by the anisotropic friction angle. This is due to the amount of stress dilatancy affected by the friction angle (see Fig. 10c). Since the
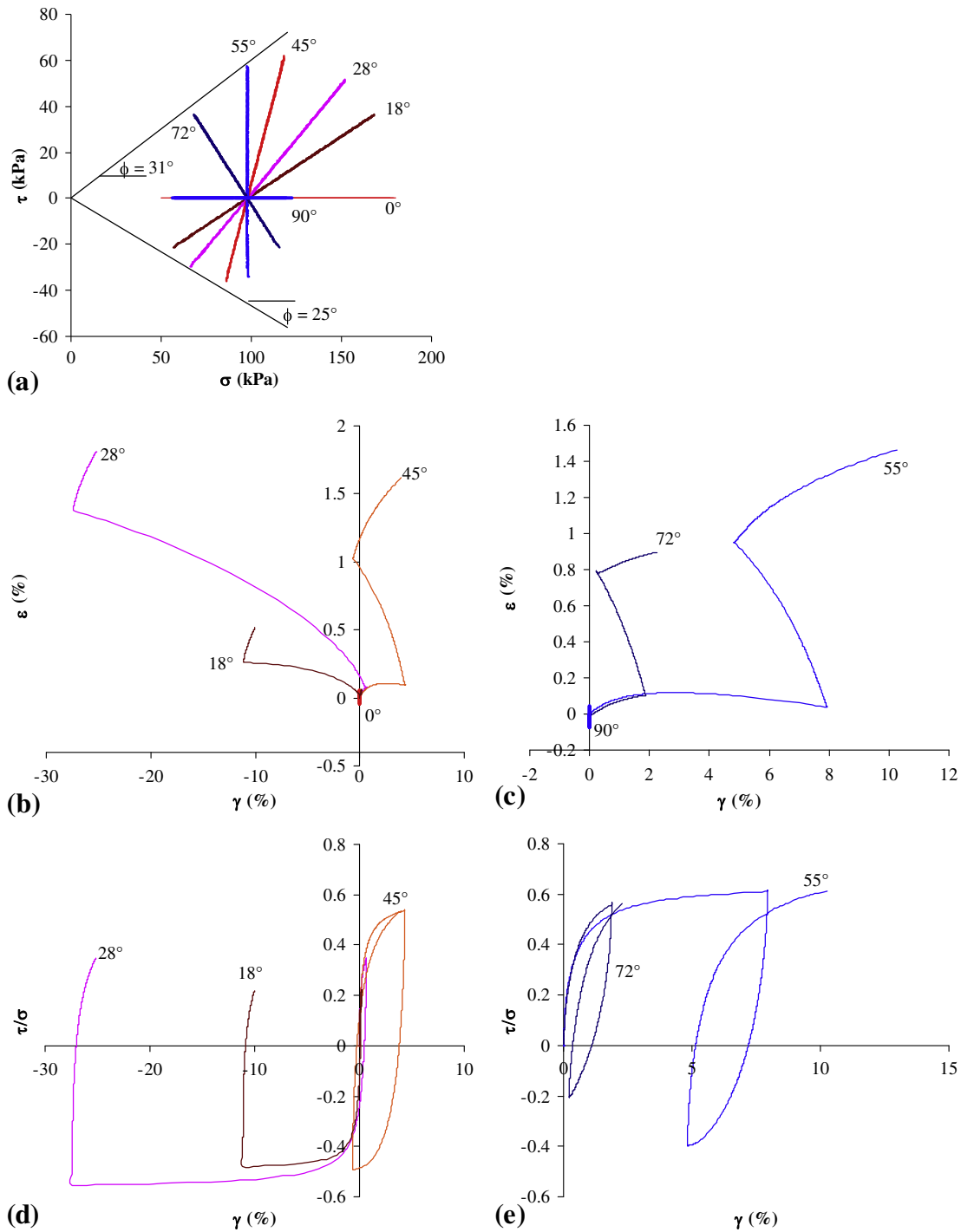
Fig. 15. Local behaviour on inter-particle planes for constant p' test with loading, unloading and reloading.

stress dilatancy is formulated by Eq. (2) for local contact planes, and each contact plane has a different value of $\tan \phi_0$ (see Fig. 9), the overall dilatancy of soil element is affected by the orientation-dependent property.

The inherent anisotropic friction angle also shows effects on the effective stress path (see Fig. 10d) and the stress–strain response (Fig. 10e) during undrained cyclic loading. The large deviatoric strain occurs starting from the ninth cycle for the case of isotropic friction angle and from the 10th cycle for the anisotropic case. In general, the deviatoric strains during cycles for anisotropic case occur with a trend of larger value in unloading than that for isotropic

case (see Fig. 10e). This is due to the smaller strength in extension for $a_0 = -0.6$ than that for $a_0 = 0$.

4. Experimental validation

4.1. Drained cyclic behaviour of Toyoura sand

4.1.1. Calibration of model parameters

Toyoura sand has a maximum void ratio of 0.977, a minimum void ratio of 0.597, and a specific gravity of 2.65. The mean size
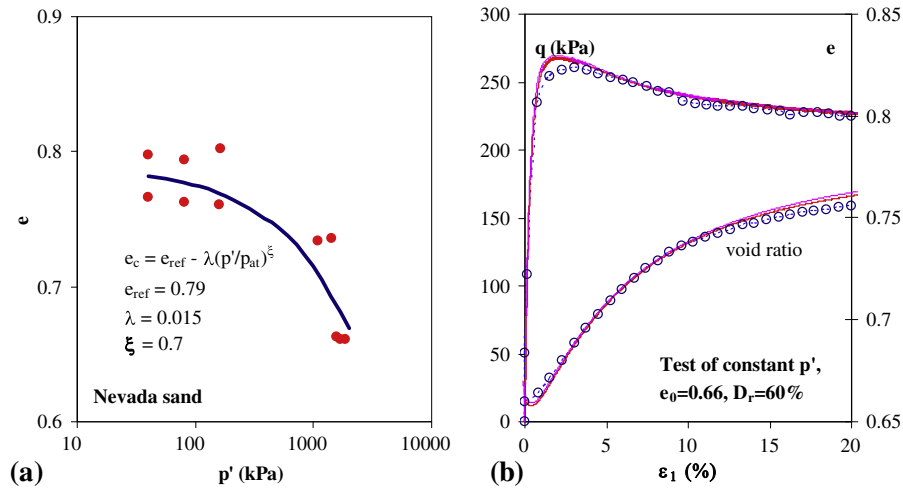
Fig. 16. Critical state line in e–$\log p'$-plane for Nevada sand.

Fig. 17. Comparison between experimental results and model predictions for undrained triaxial test under two-way cyclic loading on Nevada sand with relative density of 60%.

of the particle for the sand is $d = 0.17$ mm. All values of parameters were determined as follows:

(1) The inter-particle elastic constant k_{n0} was obtained to be 12.5 N/mm and $n = 0.5$ from isotropic compression test (see Fig. 5). The parameter for inherent anisotropic stiffness a_0 can be obtained from isotropic compression test providing vertical and horizontal strains. Due to lack of data, $a_0 = 0.6$ was assumed (for horizontal bedding planes) based on observations on shear modulus in compression and extension conditions by Pradhan et al. (1989).
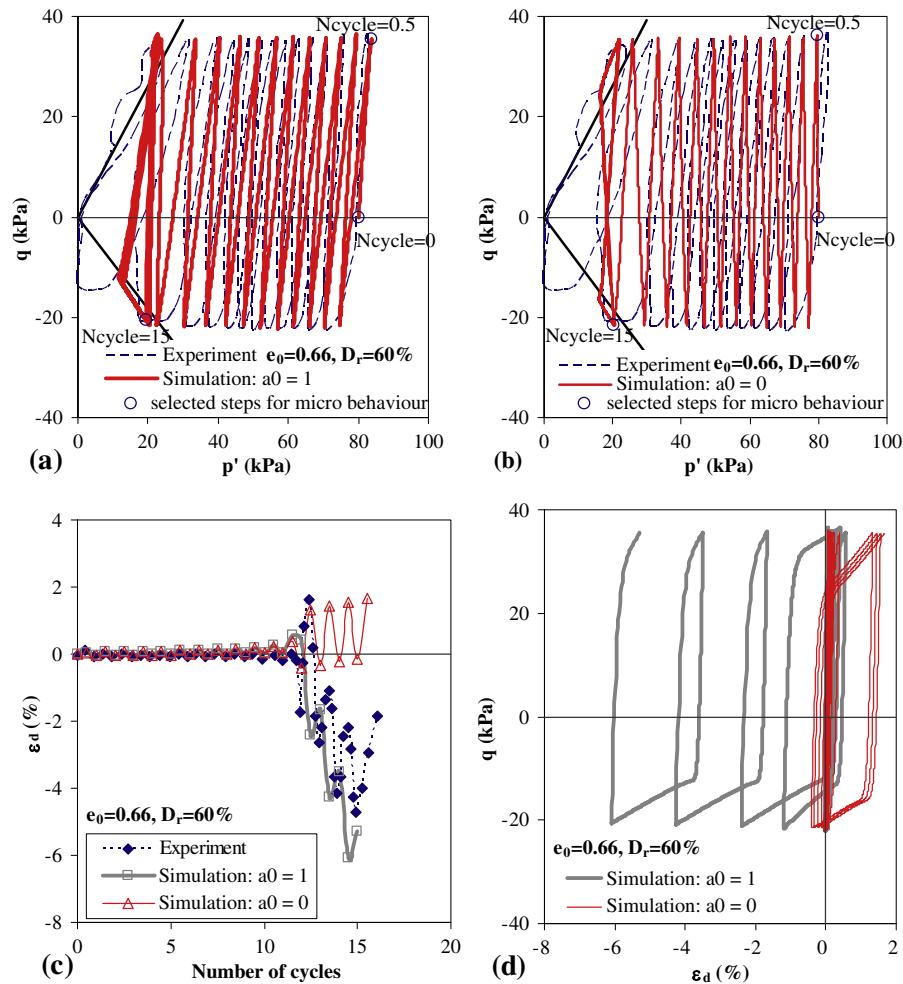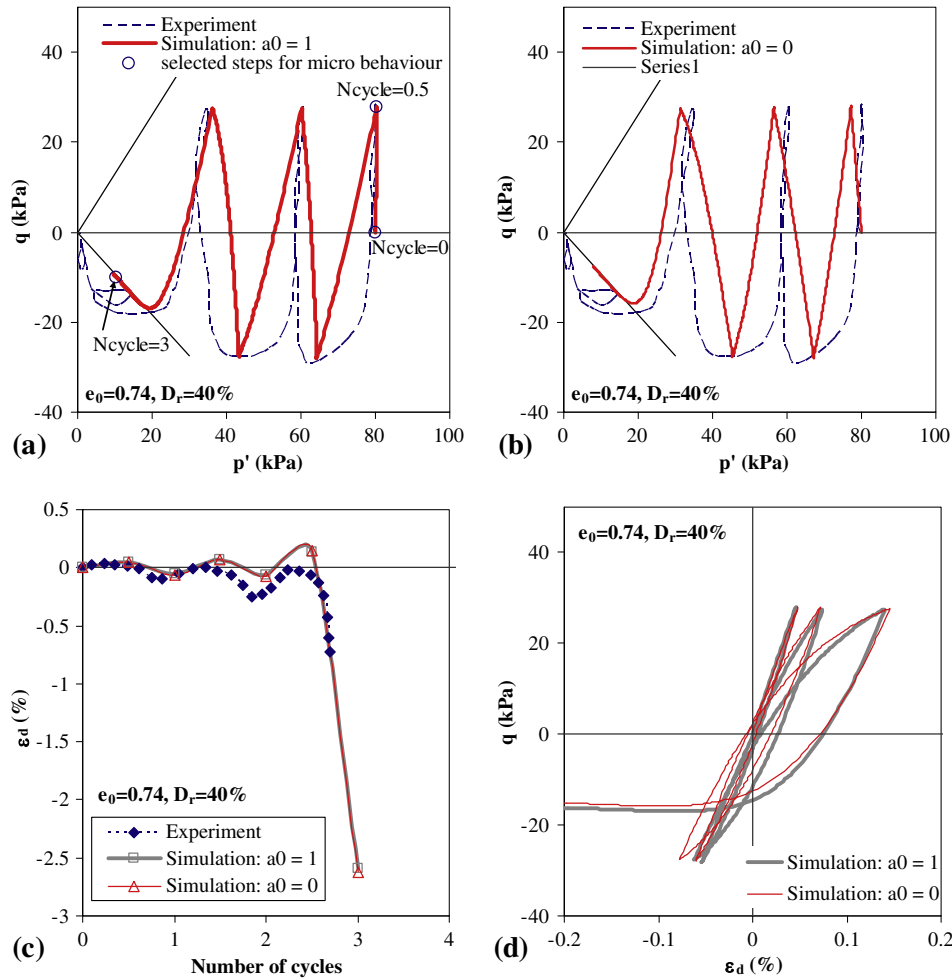
Fig. 18. Comparison between experimental results and model predictions for undrained triaxial test under two-way cyclic loading on Nevada sand with relative density of 40%.

(2) The parameters for critical state line were obtained from test results by Verdugo and Ishihara (1996): $e_{ref} = 0.934$, $\lambda = 0.019$, and $\xi = 0.7$ (see Fig. 5).

(3) $k_{pR} = 0.15$ was determined from the stress–strain curve of first loading stage.

(4) The internal friction angle $\phi_\mu = 31°$ with its anisotropic parameter $a_0 = -0.3$ (for horizontal bedding planes) was obtained by simulating stress–strain curves for all three stages (see Fig. 11a).

(5) The dilatancy parameters $D = 1$ and $h = 5$ were determined from curve fitting the evolution of stress dilatancy for all three stages (see Fig. 11b) according to parametric study (see Fig. 6).

The set of parameters for Toyoura sand is presented in Table 1, which is then used to predict other drained cyclic tests on the same material.

4.1.2. Simulations for drained cyclic tests

Fig. 12 shows comparisons between experiments and predictions for the drained cyclic triaxial test on loose Toyoura sand with void ratio $e_{0.3} = 0.845$ under constant $p' = 98$ kPa. Fig. 13 shows comparisons for a dense Toyoura sand with void ratio $e_{0.3} = 0.653$ under constant $p' = 98$ kPa. Good agreement was achieved between experimental data and simulations. The over-prediction for the volumetric strain at the third cycle is maybe caused by sample

variations since the values of parameters used for predicting this test are determined from a different test. The enhanced model well captured the trend: at small strain amplitude, loose sand densifies and dense sand dilates.

Fig. 14 shows comparisons between experiments and predictions for four drained cyclic triaxial tests on loose Toyoura sand with void ratio $e_{0.3} = 0.832-0.865$ under four different confining pressure $p' = 24.5, 49, 98, 147$ kPa. Simulations agrees with experimental data for both curves of stress ratio versus deviatoric strain and the evolution of dilatancy ratio ($d = d\varepsilon_v^p/d\varepsilon_d^p$) versus stress ratio during cyclic loading. The effect of mean effective stress p' on drained cyclic behaviour was well captured by the enhanced model.

4.1.3. Local stress–strain behaviour

In this section, we investigate the predicted local stress–strain behaviour for contact planes. Since the applied loading is axi-symmetric about x-axis, the orientation of a given contact plane can be represented by inclined angle, θ, which is measured between the branch vector and the x-axis of the coordinate system as shown in Fig. 1. Seven contact planes were selected for this investigation with inclined angles $\theta = 0°, 18°, 28°, 45°, 55°, 72°$ and $90°$ ($\theta = 0°$ corresponds to a horizontal contact plane), as shown, respectively, in the x–z-plane on Fig. 1. The test with loading, unloading and reloading (see Fig. 11) was selected to investigate the local behaviour of contact planes.

In order to obtain a more direct comparison between the local behaviour and the overall stress–strain behaviour, in the following discussions, we use the variables of local strain and local stress as normalized inter-particle force and inter-particle displacement. For this purpose, we define a local normal stress $\sigma^\alpha = f_n^\alpha N l / 3V$ and a local shear stress $\tau^\alpha = f_r^\alpha N l / 3V$, where l is branch length and N/V is the total number of contact per unit volume. The corresponding local normal strain is defined as $\varepsilon^\alpha = \delta_n^\alpha / l$ and a local shear strain is defined as $\gamma^\alpha = \delta_r^\alpha / l$. With these definitions, applying

static hypothesis for an isotropic material, the local stress and overall stress are related by $\tau_i = \sigma_{ij} n_j$, and the local strain and overall strain are related by $\gamma_i = \varepsilon_{ij} n_j$.

The local stress paths for the seven selected contact orientations are plotted in Fig. 15(a). The local stress paths for all contact planes are different each other. The 28° contact planes reach the internal friction line in extension (see Fig. 15d, $\phi = 24°$); the 55° contact planes reach the internal friction line in compression (see Fig. 15e, $\phi = 31°$). For the 0° and 90° contact planes, shear stress
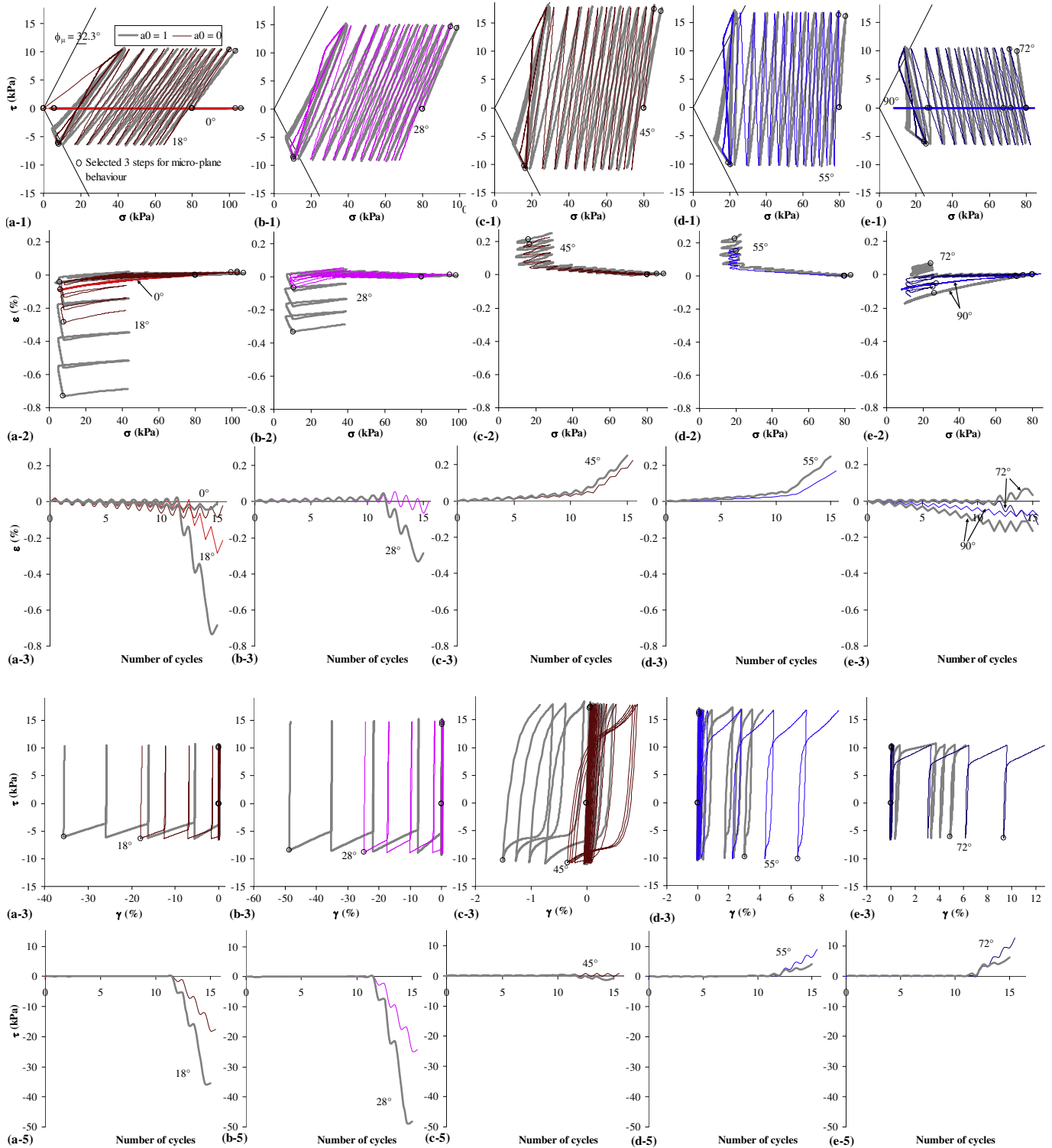

Fig. 19. Local behaviour on seven different inter-particle planes for undrained triaxial test under cyclic loading on Nevada sand with relative density of 60%.

is null. Different internal friction angles for different planes are due to inherent anisotropy of friction angle.

Fig. 15(b) and (c) shows curves of local normal strain versus shear strain. Some contact planes show shear strain in positive (18°, 28°) and some contact planes in negative (45°, 55°, 72°). Null shear strain occurs for plane 0° and 90° since there is no shear stress on these two contact planes. In general, all contact planes behave contraction during three loading stages.

Fig. 15(d) and (e) shows curves of local stress ratio versus shear strain. The accumulated strains in some plane orientations tends to be positive (18°, 28°); some others tend to be negative (45°, 55°, 72°). The planes with largest movements are near the orientation of 28° (close to $\pi/4 - \phi_\mu^{ave}/2 = 29.5°$) during unloading, and near the orientation of 55° (close to $\pi/4 + \phi_\mu^{ave}/2 = 60.5°$) during loading. The figures also clearly indicate that every contact plane is mobilized to a different degree of strain and in a different direction.

4.2. Undrained cyclic behaviour of Nevada sand

Arulmoli et al. (1992) performed undrained triaxial tests under cyclic loading on Nevada sand with two different relative densities (D_r = 60% and D_r = 40%). In this paper, both densities are selected for analysis. To compare the effect of inherent anisotropy on undrained cyclic behaviour, both isotropy and inherent anisotropy are considered in the predictions.

4.2.1. Model parameters

The mean size of the particle for Nevada sand is d = 0.15 mm. Due to lack of results of isotropic compression test, the inter-particle elastic constant k_{n0} = 9.8 N/mm is assumed with exponent n = 0.5, which is a typical value for sand (see Chang and Hicher, 2005). The value of k_{rR} is taken equal to 0.4. From the results of critical state void ratios in Fig. 16(a), the parameters for the critical state in the e–p'-plane were obtained: λ = 0.015, e_{ref} = 0.79 and ξ = 0.7. The value of k_{pR} = 0.3 was obtained from initial slope of stress–strain curves of monotonic test (p'-constant test shown in Fig. 16b). h = 5 and D = 2 were obtained from drained cyclic tests. The set of parameters for Nevada sand is presented in Table 1.

The two soil samples with different relative densities were isotropically consolidated up to 80 kPa. Afterwards, both samples were deviatorically and cyclically loaded in undrained condition. In order to investigate the influence of inherent anisotropy, we assign the following anisotropy of the elastic constant: $k_{n0}^1 = 200$ and $k_{n0}^2 = k_{n0}^3 = 50$ (or $k_{n0}^{ave} = 100$ and a_0 = 1). Since the particle shape of Nevada sand is relatively round, the friction angle is considered inherently isotropic. The inherent anisotropic stiffness does not seem to change the prediction for the monotonic p'-constant test (see Fig. 16b).

4.2.2. Simulations for undrained cyclic tests

Fig. 17 shows comparisons between experiments and predictions by the enhanced model considering inherent anisotropy (marked as "simulation: a_0 = 1") and not considering inherent anisotropy (marked as "simulation: a_0 = 0") for dense Nevada sand (D_r = 60%). The consideration of inherent anisotropy improves the model performance on stress path (Fig. 17a versus Fig. 17b). For the evolution of deviatoric strain with number of cycles (Fig. 17c), the model considering inherent anisotropy correctly predicted the trend. Whilst, the model with initial isotropy predicted deviatoric strains depart from test data for number of cycles more than 11. Fig. 17(d) shows the curves of deviatoric stress versus deviatoric strain for two predictions. The evolution of stress–strain during cyclic loading tends to follow two different directions for the two cases, which is consistent with the evolution of deviatoric strain with number of cycles shown in Fig. 17(c).

Fig. 18 shows comparisons for undrained cyclic test on loose Nevada sand (D_r = 40%). In this case, both predictions with or without inherent anisotropy captured the dynamic liquefaction of loose sand under undrained condition. Different from the previous case of dense sand, the consideration of inherent anisotropy improves only the stress path. For the evolution of deviatoric strain versus number of cycles, both predictions are in agreement with the trend of experiment. The evolution of stress–strain during cyclic loading (Fig. 18d) is slightly different between two cases, which is consistent with Fig. 18(c).

4.2.3. Local stress–strain behaviour for undrained cyclic tests

In this section, we investigate the predicted local stress–strain behaviour for selected contact planes with inclined angles θ = 0°, 18°, 28°, 45°, 55°, 72° and 90°. The local behaviour of contact planes discussed here includes cyclic tests on both dense and loose samples. In order to study the evolution of local stresses and strains, we have, in each test, selected three load steps (see Figs. 17(a) and (b) and 18(a)), which are marked by hollow circles to indicate: initial step, end step of first load cycle and the step when stress path reaching internal friction line. For dense and loose sand, plots are made for local stress–strain curves and Rose diagram of anisotropic properties.

4.2.3.1. Local stress–strain behaviour for dense sand. The simulated cyclic test results are plotted in Fig. 19 for the case of inherent
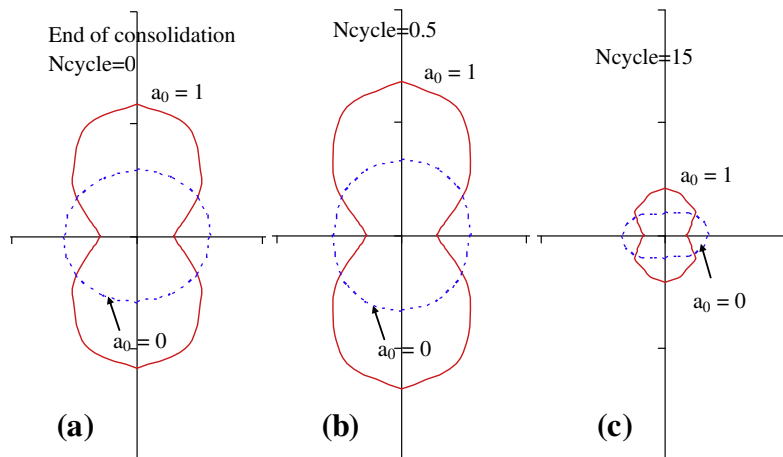

Fig. 20. Rose diagram for normal modulus of selected steps during cyclic loading.
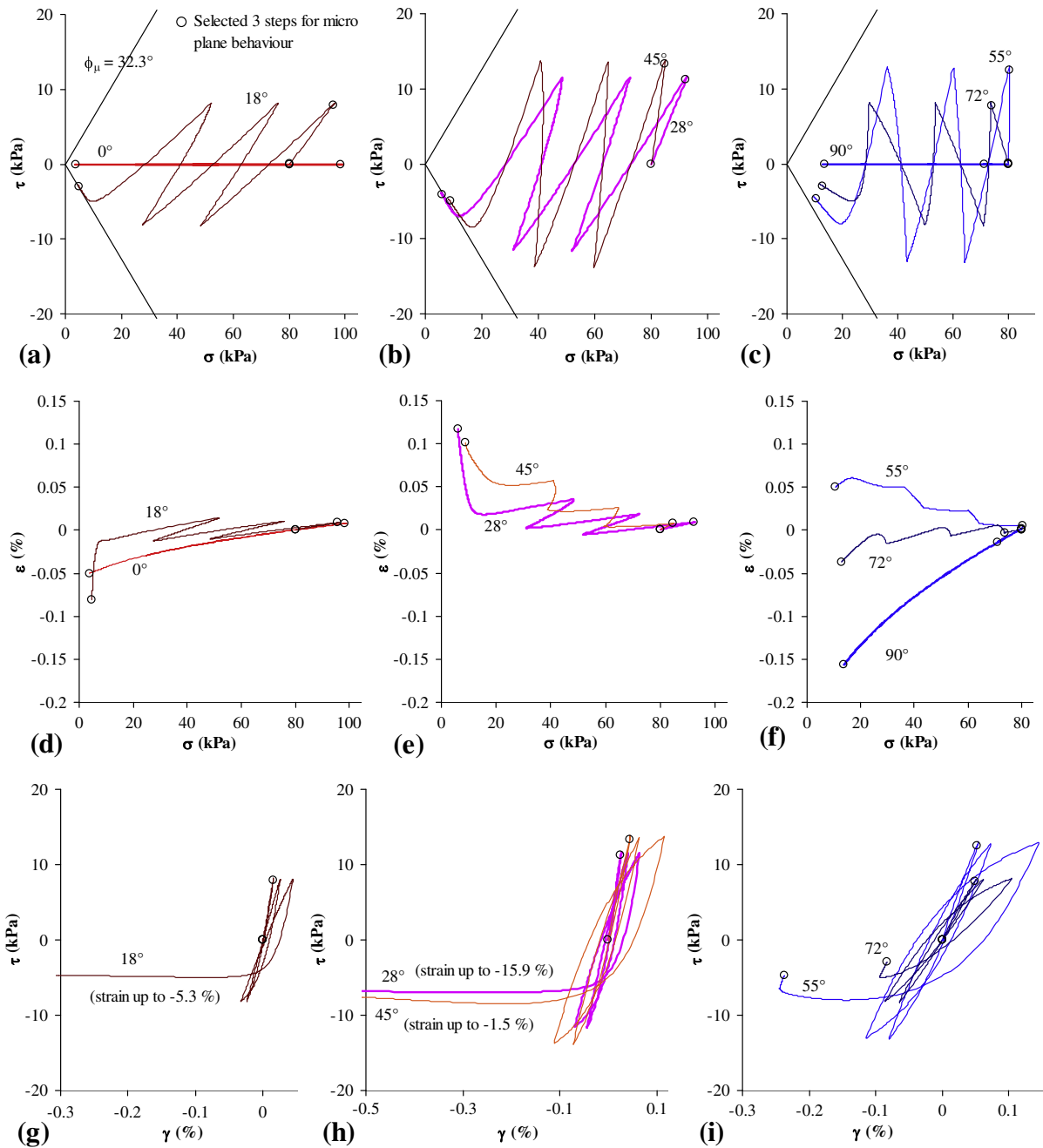
Fig. 21. Local behaviour on seven different inter-particle planes for undrained triaxial test under cyclic loading on Nevada sand with relative density of 40%.

anisotropy (marked as "$a_0 = 1$") and for the case of isotropy (marked as "$a_0 = 0$").

The local stress paths for the seven selected contact orientations are plotted in Fig. 19(a-1)–(e-1). For both cases, only the 18° and 28° contact planes reach the internal friction line in positive shear; only the 55° and 72° contact planes reach the internal friction line in negative shear; the 45° contact plane reaches the internal friction line in both positive and negative shear. For the 0° (Fig. 19(a-1)) and 90° (Fig. 19(e-1)) contact planes, shear stress is null. The differences between inherent anisotropic and isotropic cases for different planes are similar to that of global behaviours in Fig. 17(a) and (b).

Fig. 19(a-2)–(e-2) shows local normal stress–strain curves. For both cases, some contact planes are in extension (0°, 18°, 28°, 90°) and some contact planes are in compression (45°, 55°). For

the 18°, 28° and 55° contact planes the inherent anisotropic case has more deformations than those of inherent isotropic case. The 45° contact plane has almost the same deformation for both cases. The 72° contact plane behaves compression for inherent anisotropic case and behaves extension for isotropic case. To more clearly describe the evolution of strains during cyclic loading, we plot local normal strains versus number of cycles shown in Fig. 19(a-3)–(e-3).

Fig. 19(a-4)–(e-4) shows local shear stress–strain curves. For both cases, the accumulated strains in some plane orientations tends to be in positive shear (18°, 28°); some others tend to be in negative shear (55°, 72°). The inherent anisotropic case, when compared with isotropic case, gives more shear strains in positive side and less strains in negative side for all orientations. For 45° contact plane, both cases show small strains but in different
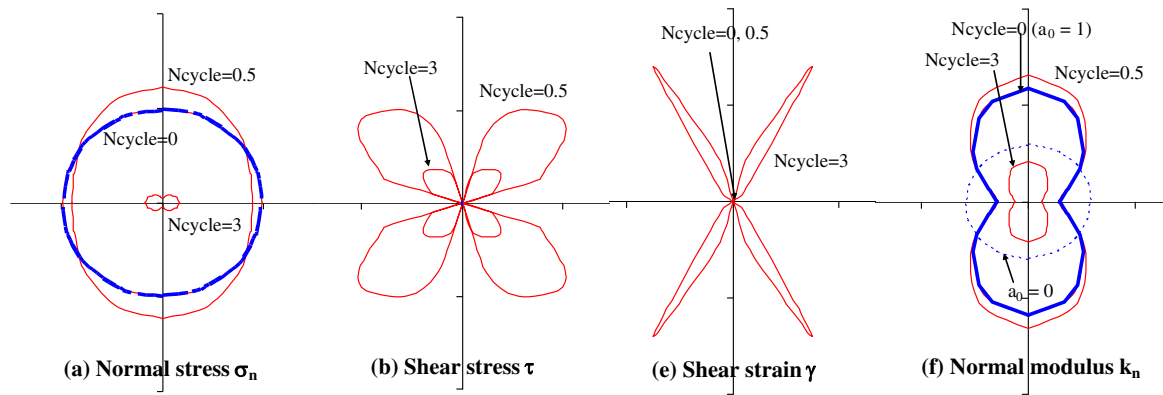
Fig. 22. Rose diagram for anisotropic behaviour of selected steps during cyclic loading.

directions. The planes with largest movements are near the orientation of 28° (close to $\pi/4 - \phi_\mu/2 = 29°$) for both cases. Similar to normal strains, we plot local shear strains versus number of cycles shown in Fig. 19(a-5)–(e-5). These figures indicate that the accumulated shear strains for all contact planes suddenly become large when the number of cycles reaches to 11.

4.2.3.2. Orientation distributions of normal modulus k_n for dense sand. Orientation distributions are plotted in X–Z-coordinate system as shown in Fig. 1. Fig. 20(a) gives the initial orientation distributions of k_n where the axes of anisotropy of the soil coincide to those of the axes of loading stresses. The given inherent anisotropic material ($a_0 = 1$) has a long axis in the vertical direction and short axis in the horizontal direction. The given isotropic material ($a_0 = 0$) has a circular shape implying isotropic distribution. During the first loading (Ncycle = 0.5 in Fig. 20b), because of the contact force-dependent property, the axis in the vertical direction becomes longer due to the increase of vertical stress for both cases. For Ncycle = 15 in Fig. 20(c), k_n for both cases becomes smaller when stresses reduce as pore pressure build-up during undrained cyclic loading. The long axis, for the isotropic case, is changed to horizontal direction since the stress state is in extension for the selected step. For the inherent anisotropic case, the long axis is still kept but the ratio of long axis to short axis becomes smaller due to the stress-dependency of k_n.

In the present model, the forces on each plane are considered as internal state variables, and their evolution can serve to model the behaviour change on each individual plane, thus the results exhibit naturally the stress-induced anisotropy.

4.2.3.3. Local stress–strain behaviour for loose sand. We plot the simulated cyclic test on loose sand in Fig. 21 for the case of inherent anisotropy (marked as "$a_0 = 1$").

The local stress paths for the seven selected contact orientations are plotted in Fig. 21(a)–(c) in three groups: (a) 0°, 18°, (b) 45°, 28°, and (c) 55°, 72°, 90°. The 18°, 28° and 45° contact planes reach the internal friction line in positive shear and tend to liquefy, while others do not. Fig. 21(d)–(f) shows local normal stress–strain curves. Some contact planes are in extension (0°, 18°, 72°, 90°) and others are in compression (28°, 45°, 55°), similar to the previous case of dense sand. Fig. 21(g)–(i) shows local shear stress–strain curves which indicates that every contact plane is mobilized to a different degree. The planes with largest movements are near the orientation of 28° (close to $\pi/4 - \phi_\mu/2 = 29°$).

4.2.3.4. Orientation distributions of local stresses and strains for loose sand. Fig. 22 shows the distributions of local stresses and strains at contact planes of various orientations (in Rose diagram). It is

plotted for the end step of isotropic consolidation (see Ncycle = 0 in Fig. 13), and the subsequent two selected load steps:

(1) The distribution of *normal stress* σ at the end of isotropic consolidation has a circular shape (see the bold line in Fig. 22a) which implies an isotopic distribution of normal stress for all plane contacts. For the first loading, the normal stress in vertical direction becomes larger and horizontal direction becomes smaller. Then during the cyclic loading, the pore pressure is developed thus the distribution shrinks from step "Ncycle = 0.5" to step "Ncycle = 3" with the long axis in the horizontal direction (i.e., more reduction of normal stress at the contact planes of vertical orientation).

(2) The distribution of *shear stress* τ expands from 0 to step "Ncycle = 0.5" and then reduces to step "Ncycle = 3" with a similar shape of distribution (Fig. 22b).

(3) The distribution of *shear strain* γ in Fig. 22(c) shows that very large strains have occurred at step "Ncycle = 3" for the contact planes near the orientation of 28°, which agrees with local stress–strain behaviour (Fig. 21h).

(4) The distribution of *normal modulus* k_n in Fig. 22(d) shows that the stiffness is kept anisotropic with long axis of vertical direction even its values are changed with normal stress. Due to stress-induced anisotropy, the ratio of long axis to short axis becomes smaller for the selected step "Ncycle = 3".

5. Conclusions and discussions

A new micromechanical stress–strain model has been extended following the approach proposed by Chang and Hicher (2005). The model takes into account the behaviour of stress reversal on a contact plane and the effect of density state on dilatancy. This feature is needed for the model in order to simulate experimental tests subjected to cyclic loadings.

The model was first examined by a parametric study for typical drained and undrained cyclic tests in conventional triaxial conditions. The effects of dilatancy constants and inherent anisotropy (for stiffness and for friction angle) were investigated.

The model applicability was then evaluated by comparing the predictions and experimental results for two different sands: Toyoura sand and Nevada sand. The predictions show good agreement with experimental measurements on sand with different initial void ratios and different level of p'. Inherent anisotropy of stiffness and friction angle was found necessary to be considered. The model well captured the trend of drained cyclic behaviour.

Furthermore, in the predictions for undrained triaxial tests on dense and loose Nevada sand under cyclic loading were made

considering both isotropy and anisotropy of stiffness. Comparisons also show that the inherent anisotropy of stiffness is necessary to be considered for modelling the selected tests. The model well captured the accumulation of strains for dense sand and the liquefaction for loose sand during cyclic loading.

The predicted behaviour of contact planes has been examined for three stages: loading, unloading and reloading stages, for dense sand and loose sand under drained and undrained cyclic loading. For the case of drained triaxial test, we concentrated to investigate the influence of the inherent anisotropy of friction angle on the overall stress–strain behaviour. For undrained case, more attention was paid on the effect of inherent anisotropy of stiffness and stress-induced anisotropy. It has been shown from the Rose diagrams that the shape of contact stress distribution and normal modulus changes throughout the triaxial test, which clearly indicates the development of anisotropy induced by the externally applied load, since the properties on each contact plane are force-dependent. For both drained and undrained cases, the local stress–strain response on contact planes has shown that every contact plane is mobilized to a different degree. A few active contact planes contribute largely to the deformation of the assembly, while most contact planes are inactive and have small movement. Therefore, the local strains are highly non-uniform.

Model predictions for drained cyclic tests on Toyoura sand and undrained cyclic tests on Nevada sand have demonstrated that the present micromechanical approach is capable of modelling the cyclic behaviour of sand with inherent and induced anisotropy.

Appendix A. Micromechanics-based model

The micromechanics-based model in this paper is extended from the model for sand developed by Chang and Hicher (2005).

A.1. Inter-particle behaviour

A.1.1. Elastic stiffness

On each contact plane, an auxiliary local coordinate can be established as shown in Fig. 1 where n, s, t are three orthogonal unit vectors that form the local coordinate system. The vector n is outward normal to the contact plane. Vectors s and t are on the contact plane. The contact stiffness of a contact plane includes normal stiffness, k_n^α, and shear stiffness, k_r^α. The elastic stiffness tensor is defined by

$$f_i^\alpha = k_{ij}^{\alpha e} \delta_j^{\alpha e} \tag{A1}$$

which can be related to the contact normal and shear stiffness

$$k_{ij}^{\alpha e} = k_n^\alpha n_i^\alpha n_j^\alpha + k_r^\alpha \left(s_i^\alpha s_j^\alpha + t_i^\alpha t_j^\alpha \right) \tag{A2}$$

The superscript α represents the term at the αth contact plane; $k_{ij}^{\alpha e}$ and $\delta_{ij}^{\alpha e}$ represent the elastic stiffness tensor and elastic displacement tensor at the αth contact plane. In the remaining section for the inter-particle behaviour, the superscript α is neglected in order to simplify the writing.

The value of the stiffness for two elastic spheres can be estimated from Hertz–Mindlin's formulation (1969). For sand grains, a revised form was adopted (Chang et al., 1989), given by

$$k_n = k_{n0} \left(\frac{f_n}{f_{\mathrm{ref}}} \right)^n ; \quad k_r = k_{rR} k_{n0} \left(\frac{f_n}{f_{\mathrm{ref}}} \right)^n \tag{A3}$$

where f_{ref} is the reference value by $f_{\mathrm{ref}} = \frac{3V}{Nl} p_{\mathrm{at}}$ (p_{at} is atmosphere pressure equal to 101.3 kPa, N is the total number of contacts and V is volume), f_n is the contact force in normal direction. l is the branch length between the two particles. k_{no}, k_{rR} and n are material constants. For two spherical particles, the branch length is same as particle size $l = d$. Let $n = 1/3$, and given k_{n0} an appropriate function

of particle size and modulus, Eq. (A3) can be made equivalent to the Hertz–Mindlin's contact formulation (Hicher and Chang, 2006).

A.1.2. Plastic yield and hardening functions

The yield function is assumed to be of Mohr–Coulomb type, defined in a contact force space (e.g., f_n, f_s, f_t).

$$F(f_n, f_r, \kappa) = \frac{f_r}{f_n} - \kappa(\delta_r^p) \tag{A4}$$

where $\kappa(\delta_r^p)$ is a hardening/softening function. When $dF > 0$, it indicates loading, otherwise unloading. Note that the shear force f_r and the rate of plastic sliding δ_r^p can be defined as

$$f_r = \sqrt{f_s^2 + f_t^2} \quad \text{and} \quad \delta_r^p = \sqrt{\left(\delta_s^p\right)^2 + \left(\delta_t^p\right)^2} \tag{A5}$$

The hardening function is defined by a hyperbolic curve in $\kappa-\delta_r^p$-plane, which involves two material constants: ϕ_p and k_{p0}.

$$\kappa = \frac{k_{p0} \tan \phi_p \delta_r^p}{\tan \phi_p + k_{p0} \delta_r^p} \tag{A6}$$

The value of κ asymptotically approaches the apparent inter-particle friction angle $\tan \phi_p$. The initial slope of the hyperbolic curve, k_{p0} is proposed to relate f_n and k_n by a constant k_{pR}:

$$k_{p0} = k_{pR} k_n / f_n \tag{A7}$$

A.1.3. Plastic flow rule

The elastic sliding behaviour between two particles does not have a coupling effect (i.e., there is no shear-induced normal movements). However, the plastic sliding often occurs along the tangential direction of the contact plane with an upward or downward movement, thus the shear-induced dilation/contraction takes place. The shear-induced dilatancy is a well-known phenomenon in sand (see discussions in the work by Taylor (1948), Rowe (1962) and Goddard and Bashir (1990)), and should be correctly modelled. The following flow rule was used in the model of Chang and Hicher (2005):

$$\begin{Bmatrix} d\delta_n^p \\ d\delta_s^p \\ d\delta_t^p \end{Bmatrix} = d\delta_r^p \begin{Bmatrix} D\left[\tan\phi_0 - \frac{1}{\tan\phi_m}\left(\frac{f_s}{f_n}\right)^2 - \frac{1}{\tan\phi_m}\left(\frac{f_t}{f_n}\right)^2\right] \\ \frac{1}{\tan\phi_m}\frac{f_s}{f_n} \\ \frac{1}{\tan\phi_m}\frac{f_t}{f_n} \end{Bmatrix} \tag{A8}$$

where

$$\tan\phi_m = \sqrt{\left(\frac{f_s}{f_n}\right)^2 + \left(\frac{f_t}{f_n}\right)^2} \tag{A9}$$

Eq. (A8) leads to a dilatancy relation at a contact plane in a similar form to that proposed by Taylor (1948)

$$\frac{d\delta_n^p}{d\delta_r^p} = D\left(\tan\phi_0 - \frac{f_r}{f_n}\right) \tag{A10}$$

where D is material constant for stress dilatancy, the material constant ϕ_0 was considered equal to the inter-particle friction angle ϕ_μ. This equation can be derived by assuming that the dissipation work for a contact plane due to both normal and shear plastic movements $(f_n d\delta_n^p + f_r \delta_r^p D)$ is equal to the energy loss due to friction $(f_n \tan\phi_0 d\delta_r^p D)$ at the contact. The dilatancy equation shown in Eq. (A10) implies a non-associated plastic flow rule for sand.

In Eq. (A10), the $\tan\phi_0$ also represents the slope of the phase transformation line, defined by Ishihara et al. (1975), at which the plastic volumetric strain rate is zero; or represents "characteristic state" as defined by Luong (1979).

A.1.4. Elasto-plastic relationship

With the elastic and plastic behaviour described above, the final incremental force–displacement relationship of the inter-particle contact can be derived, given by

$$\dot{f}_i^\alpha = k_{ij}^\alpha \dot{\delta}_j^\alpha \tag{A11}$$

Detailed expression of the elasto-plastic stiffness tensor can be derived from yield function and flow rule (see Chang and Hicher, 2005), in which k_{ij}^α, is functions of k_{n0}, k_{rR}, k_{pR}, $\tan\phi_p$, D and f_r/f_n. The derivation is not included here.

A.2. Influence of density state

A.2.1. Density state variable

It is noted that assumptions are necessary to link the contact behaviour to assembly behaviour. In this model, a static hypothesis is used (see Section 2.1). Due to the assumption of static constraints, the interactions among particles have been neglected and the system tends to be softer than true behaviour. To account for the interactions among neighbouring particles, a density state $\varphi = e_c/e$ is introduced in reference to the void ratio at critical state.

Soil is said to be in critical state when it undergoes large shear deformations at a constant volume and a constant stress state (Schofield and Wroth, 1968). The void ratio corresponding to this state is e_c. A locus of critical states can be plotted in a three-dimensional space consisting of deviatoric stress, mean stress, and void ratio. The locus is called a critical state line (CSL). The projection of CSL on the plane of mean stress and void ratio represents the critical void ratio e_c as a function of the mean stress, which can be written as follows for sand:

$$e_c = e_{\mathrm{ref}} - \lambda\left(\frac{p'}{p_{\mathrm{at}}}\right)^\xi \tag{A12}$$

where ξ and λ are two material constants, p' is the mean effective stress of the packing.

A.2.2. Effect of density state on the apparent friction angle (ϕ_p)

Resistance against sliding on a contact plane is dependent on the degree of interlocking by neighbouring particles. The resistance can be related to the state of packing void ratio e by (Biarez and Hicher, 1994):

$$\tan\phi_p = \left(\frac{e_c}{e}\right)^m \tan\phi_\mu \tag{A13}$$

where m is a material constant (Biarez and Hicher, 1994), which is typically equal to 1. For dense packing, the apparent inter-particle friction angle ϕ_p is greater than the internal friction angle ϕ_μ. When the packing structure dilates, the degree of interlocking and the apparent frictional angle are reduced, which results in a strain-softening phenomenon. For loose packing, the apparent frictional angle ϕ_p is smaller than the internal friction angle ϕ_μ.

A.3. Overall stress–strain relationship

A.3.1. Macro–micro relationship

The stress–strain relationship for an assembly can be determined from integrating the behaviour of inter-particle contacts in all orientations. In the integration process, a micro–macro relationship is required. Using the static hypothesis, we obtain the relation between the global strain and inter-particle displacement.

$$\dot{u}_{j,i} = A_{ik}^{-1} \sum_{\alpha=1}^{N} \dot{\delta}_j^\alpha l_k^\alpha \tag{A14}$$

where the branch vector l_k^α is defined as the vector joining the centres of two particles, and the fabric tensor is defined as

$$A_{ik} = \sum_{\alpha=1}^{N} l_i^\alpha l_k^\alpha \tag{A15}$$

The mean force on the contact plane of each orientation is

$$\dot{f}_j^\alpha = \dot{\sigma}_{ij} A_{ik}^{-1} l_k^\alpha V \tag{A16}$$

The stress increment can be obtained by the contact forces and branch vectors for all contacts (Christofferson et al., 1981; Rothenburg and Selvadurai, 1981), as follows:

$$\dot{\sigma}_{ij} = \frac{1}{V} \sum_{\alpha=1}^{N} \dot{f}_j^\alpha l_i^\alpha \tag{A17}$$

Apply Eq. (A17) to the stress in Eq. (A16), it can be observed that Eq. (A16) is satisfied automatically.

A.3.2. Stress–strain relationship

Using Eqs. (A14), (A11), and (A16), the following relationship between stress increment and strain increment can be obtained:

$$\dot{u}_{i,j} = C_{ijmp}\dot{\sigma}_{mp}; \quad \text{where} \quad C_{ijmp} = A_{ik}^{-1} A_{mn}^{-1} V \sum_{\alpha=1}^{N} \left(k_{jp}^{ep}\right)^{-1} l_k^\alpha l_n^\alpha \tag{A18}$$

When the contact number N is sufficiently large in an isotropic packing, the summation of flexibility tensor in Eq. (A18) and the summation of fabric tensor in Eq. (A15) can be written in integral form, given by

$$C_{ijmp} = A_{ik}^{-1} A_{mn}^{-1} \frac{NV}{2\pi} \int_0^{\pi/2} \int_0^{2\pi} k_{jp}^{ep}(\theta,\beta)^{-1} l_k(\theta,\beta) l_n(\theta,\beta) \sin\theta\, d\theta\, d\beta \tag{A19}$$

and

$$A_{ik} = \frac{N}{2\pi} \int_0^{\pi/2} \int_0^{2\pi} l_i(\theta,\beta) l_k(\theta,\beta) \sin\theta\, d\theta d\beta \tag{A20}$$

The integration of Eqs. (A19) and (A20) in a spherical coordinate can be carried out numerically using Gauss integration points over the surface of the sphere.

The total number of contacts per unit volume changes during the deformation. Using the experimental data by Oda (1977) for three mixtures of spheres, the total number of contact per unit volume can be approximately related to the void ratio by the following expression by Hicher and Chang (2006):

$$\frac{N}{V} = \left(\frac{N}{V}\right)_0 \frac{(1+e_0)e_0}{(1+e)e} \tag{A21}$$

This equation is used to account for the evolution of contact number per unit volume. The initial contact number per unit volume can be obtained by

$$\left(\frac{N}{V}\right)_0 = \frac{3C_n}{\pi d^3(1+e_0)} \tag{A22}$$

where d is the mean particle size and C_n is the average co-ordination number, which can be approximated for the range of $e = 0.38$–0.87 by (see Chang and Misra, 1990)

$$C_n = 13.28 - 8e_0. \tag{A23}$$

References

Anandarajah, A., 2008. Modeling liquefaction by a multimechanism model. ASCE Journal of Geotechnical and Geoenvironmental Engineering 134 (7), 949–959.

Arulmoli, K., Muraleetharan, K.K., Hossain, M.M., Fruth, L.S., 1992. VELACS: verification of liquefaction analysis by centrifuge studies, laboratory testing program, soil data report. Technical Report, The Earth Technology Corporation, Irvine, California.

Balendran, B., Nemat-Nasser, S., 1993. Double sliding model for cyclic deformation of granular materials including dilatancy effects. Journal of the Mechanics and Physics of Solids 41 (3), 573–612.

Bardet, J.P., 1985. Application of bounding surface plasticity to cyclic sand behavior. In: Proceeding of Second International Conference on Soil Dynamics and Earthquake Engineering, vol. 2, Springer, Berlin, pp. 3–16.

Biarez, J., Hicher, P.Y., 1994. Elementary Mechanics of Soil Behaviour. Balkema, Amsterdam. p. 208.

Chang, C.S., Hicher, P.Y., 2005. An elastic–plastic model for granular materials with microstructural consideration. International Journal of Solids and Structures 42 (14), 4258–4277.

Chang, C.S., Misra, A., 1990. Application of uniform strain theory to heterogeneous granular solids. ASCE Journal of Engineering Mechanics 116 (10), 2310–2328.

Chang, C.S., Sundaram, S.S., Misra, A., 1989. Initial moduli of particulate mass with frictional contacts. International Journal for Numerical and Analytical Methods in Geomechanics 13 (6), 626–641.

Christofferson, J., Mehrabadi, M.M., Nemat-Nasser, S., 1981. A micromechanical description on granular material behaviour. ASME Journal of Applied Mechanics 48, 339–344.

Dafalias, Y.F., Herrmann, L.R., 1982. Bounding surface formulation of soil plasticity. In: Pande, G.N., Zienkiewicz, D.C. (Eds.), Soil Mechanics – Transient and Cyclic Loads. Wiley, New York, pp. 253–282.

Dakoulas, P., Yu, S., 1995. Stress-dependency of elastic moduli for cross-anisotropic soils. Géotechnique 45 (2), 325–332.

Goddard, J.D., Bashir, Y.M., 1990. On Reynolds dilatancy. In: De Kee, D., Kaloni, P.N. (Eds.), Recent Development in Structured Continua, vol. II. Longman, London, pp. 23–35.

Hicher, P.Y., Chang, C.S., 2006. Anisotropic nonlinear elastic model for particulate materials. ASCE Journal of Geotechnical and Geoenvironmental Engineering 132 (8), 1052–1061.

Hyodo, M., Tanimizu, H., Yasufuku, N., Murata, H., 1994. Undrained cyclic and monotonic triaxial behaviour of saturated loose sand. Soils and Foundations 34 (1), 19–32.

Ishihara, K., Tatsuoka, F., Yasuda, S., 1975. Undrained deformation and liquefaction of sand under cyclic stresses. Soils and Foundations 15 (1), 29–44.

Jefferies, M.G., 1993. NorSand: a simple critical state model for sand. Géotechnique 43, 91–103.

Koseki, J., Kawakami, S., Nagayama, H., Sato, T., 2000. Change of small strain quasi-elastic deformation properties during undrained cyclic torsional shear and triaxial tests of Toyoura sand. Soils and Foundations 40 (3), 101–110.

López-Querol, S., Blázquez, R., 2006. Liquefaction and cyclic mobility model for saturated granular media. International Journal for Numerical and Analytical Methods in Geomechanics 30 (5), 413–439.

Luong, M.P., 1979. Les phénomènes cycliques dans les sables. Journées de rhéologie: cycles dans les sols-rupture-instabilités, Publication 2. Vaulx-en-Velin: Ecole Nationale des Travaux Publics d'Etat.

Manzari, M.T., Dafalias, Y.F., 1997. A critical state two-surface plasticity model for sands. Géotechnique 47 (2), 255–272.

Matsuoka, H., Koyama, H., Yamazaki, H., 1985. A constitutive equation for sands and its application to analyses of rotational stress paths and liquefaction resistance. Soils and Foundations 25 (1), 27–42.

Mindlin, R.D., 1969. Microstructure in linear elasticity. Archive for Rational Mechanics and Analysis 16, 51–78.

Oda, M., 1977. Co-ordination number and its relation to shear strength of granular material. Soils and Foundations 17 (2), 29–42.

Oka, F., Yashima, A., Tateishi, A., Taguchi, Y., Yamashita, S., 1999. Cyclic elasto-plastic constitutive model for sand considering a plastic-strain dependence of the shear modulus. Géotechnique 49 (5), 661–680.

Park, I.-J., Desai, C.S., 2000. Cyclic behavior and liquefaction of sand using disturbed state concept. Journal of Geotechnical and Geoenvironmental Engineering 126 (9), 834–846.

Pradhan, T.B.S., Tatsuoka, F., Sato, Y., 1989. Experimental stress–dilatancy relations of sand subjected to cyclic loading. Soils and Foundations 29 (1), 45–64.

Qadimi, A., Coop, M.R., 2007. The undrained cyclic behaviour of a carbonate sand. Géotechnique 57 (9), 739–750.

Rothenburg, L., Selvadurai, A.P.S., 1981. Micromechanical definitions of the Cauchy stress tensor for particular media. In: Selvadurai, A.P.S. (Ed.), Mechanics of Structured Media. Elsevier, Amsterdam, pp. 469–486.

Rowe, P.W., 1962. The stress–dilatancy relations for static equilibrium of an assembly of particles in contact. Proceedings of the Royal Society of London, Series A 269, 500–527.

Schofield, A.N., Wroth, C.P., 1968. Critical State Soil Mechanics. McGraw-Hill, London.

Setouchi, H., Hashiguchi, K., Ueno, M., 2005. Prediction of the deformation behavior of sand subjected to general cyclic loading by the tangential-subloading surface model. Lowland Technology International 7 (1), 51–63.

Taylor, D.W., 1948. Fundamentals of Soil Mechanics. Wiley, New York.

Verdugo, R., Ishihara, K., 1996. The steady state of sandy soils. Soils and Foundations 36 (2), 81–91.

Wan, R.G., Guo, P.J., 2001. Drained cyclic behavior of sand with fabric dependence. Journal of Engineering Mechanics 127 (11), 1106–1116.

Yu, H.-S., Khong, C., Wang, J., 2007. A unified plasticity model for cyclic behaviour of clay and sand. Mechanics Research Communications 34 (2), 97–114.